11-11-2017

Ion-Scale Wave Properties and Enhanced Ion Heating Across the Low-Latitude Boundary Layer During Kelvin-Helmholtz Instability

T. W. Moore
Embry-Riddle Aeronautical University, mooret14@my.erau.edu

K. Nykyri
Embry-Riddle Aeronautical University, nykyrik@erau.edu

A. P. Dimmock
Aalto University

AGU PUBLICATIONS

JGR

Journal of Geophysical Research: Space Physics

RESEARCH ARTICLE
10.1002/2017JA024591

Key Points:
- Obliquely propagating waves have more power in the MSP-like plasma regions when KHI is present
- Strong nonadiabatic heating associated with ion-scale wave activity is enhanced during intervals of Kelvin-Helmholtz instability
- The enhanced ion-scale wave activity and ion heating during KHI may explain the temperature asymmetry of cold component plasma sheet ions

Correspondence to:
T. W. Moore,
mooretommyw@gmail.com

Citation:
Moore, T. W., Nykyri, K., & Dimmock, A. P. (2017). Ion-scale wave properties and enhanced ion heating across the low-latitude boundary layer during Kelvin-Helmholtz instability. *Journal of Geophysical Research: Space Physics*, *122*. https://doi.org/10.1002/2017JA024591

Received 17 JUL 2017
Accepted 21 SEP 2017
Accepted article online 26 SEP 2017

Ion-Scale Wave Properties and Enhanced Ion Heating Across the Low-Latitude Boundary Layer During Kelvin-Helmholtz Instability

T. W. Moore[1], K. Nykyri[1], and A. P. Dimmock[2]

[1]Center for Space and Atmospheric Research, Physical Sciences Department, Embry-Riddle Aeronautical University, Daytona Beach, FL, USA, [2]Department of Electronics and Nanoengineering, School of Electrical Engineering, Aalto University, Espoo, Finland

Abstract In the Earth's magnetosphere, the magnetotail plasma sheet ions are much hotter than in the shocked solar wind. On the dawn sector, the cold-component ions are more abundant and hotter by 30–40% when compared to the dusk sector. Recent statistical studies of the flank magnetopause and magnetosheath have shown that the level of temperature asymmetry of the magnetosheath is unable to account for this, so additional physical mechanisms must be at play, either at the magnetopause or plasma sheet that contributes to this asymmetry. In this study, we perform a statistical analysis on the ion-scale wave properties in the three main plasma regimes common to flank magnetopause boundary crossings when the boundary is unstable to Kelvin-Helmholtz instability (KHI): hot and tenuous magnetospheric, cold and dense magnetosheath, and mixed (Hasegawa et al., 2004). These statistics of ion-scale wave properties are compared to observations of fast magnetosonic wave modes that have recently been linked to Kelvin-Helmholtz (KH) vortex centered ion heating (Moore et al., 2016). The statistical analysis shows that during KH events there is enhanced nonadiabatic heating calculated during ion scale wave intervals when compared to non-KH events. This suggests that during KH events there is more free energy for ion-scale wave generation, which in turn can heat ions more effectively when compared to cases when KH waves are absent. This may contribute to the dawn favored temperature asymmetry of the plasma sheet; recent studies suggest KH waves favor the dawn flank during Parker-Spiral interplanetary magnetic field.

1. Introduction

The origin of the properties of our near-Earth plasma is still not well understood —for instance, the specific entropy ($S = T/n^{2/3}$) increases by 1–2 orders of magnitude across the magnetopause that is indicative of strong nonadiabatic heating (Borovsky & Cayton, 2011). Furthermore, the magnetospheric ions are about 50 times hotter than those in the magnetosheath. There also exists a temperature and density asymmetry among the cold component ions in the magnetotail plasma sheet favoring the dawn flank—cold component ions are 30–40% hotter and more abundant at the dawn flank (Hasegawa et al., 2003; Wing et al., 2005).

There are three possible sources for these plasma sheet asymmetries: (a) seed asymmetry of the magnetosheath plasma temperature and density, (b) asymmetry of magnetopause processes favoring the dawn flank, and (c) asymmetry of some plasma sheet/magnetotail processes. Walsh et al. (2012) have shown dawn favored asymmetries in the proton densities and temperatures, as well as dusk favored asymmetries of the plasma flow speed and magnetic field strengths in the dayside magnetosheath near the magnetopause. In studies considering the entire dayside magnetosheath, the dawn flank, which is downstream of the quasi-parallel bow shock, has been shown to host a hotter and denser plasma close to the magnetopause (Dimmock et al., 2015; Dimmock, Pulkkinen, et al., 2016). However, the level of this dayside asymmetry (15%) is insufficient to account for the observed plasma sheet asymmetry (30–40%) in the magnetotail, in particular because magnetosheath plasma becomes cooler with increasing tailward distance. The dawn flank magnetosheath is also more prone to higher-amplitude magnetic field fluctuations that are further enhanced during faster solar wind velocities (Dimmock et al., 2014), which may affect the growth of the physical mechanisms at the magnetopause. In fact, in a more recent study Dimmock et al. (2017) have shown that increased amplitude ion-scale fluctuations generate larger temperature fluctuations.

The two main mechanisms that can facilitate plasma transport and heating at the Low-Latitude Boundary Layer (LLBL) are magnetic reconnection and KHI. Recently, Ma and Otto (2014) showed, using Hall-MHD simulations, that significant specific entropy increase associated with magnetic reconnection at the Earth's magnetopause is possible only if magnetosheath plasma beta is low ($\beta << 1$). Because magnetosheath beta typically is of the order of unity close to magnetopause (see Appendix A), other physical mechanisms must also be at work that contribute to the strong nonadiabatic ion heating in this region. The other possible mechanism is the KHI, which has been observed at the LLBL during northward (Eriksson, Lavraud et al., 2016; Fairfield et al., 2000; Hasegawa et al., 2004; Otto & Fairfield, 2000), southward (Hwang et al., 2011; Yan et al., 2014), and Parker-Spiral (PS) (Moore et al., 2016; Nykyri et al., 2006) interplanetary magnetic field (IMF) orientations. A recent survey of 6 years of in situ data from NASA's THEMIS (Time History of Events and Macroscale Interactions during Substorms) mission has shown that Kelvin-Helmholtz (KH) waves are frequent at the magnetopause (19% normalized occurrence rate), providing strong observational evidence as to their importance for magnetopause dynamics (Kavosi & Raeder, 2015). The spatial distribution of these KH waves observed between 2007 and 2013 using the list by Kavosi and Raeder (2015) favors the dawn flank magnetopause during the Parker-Spiral (PS) IMF orientation. Also, MHD simulations demonstrate that for a variety of solar wind plasma conditions and during PS IMF orientation, the KHI growth shows a slight preference for the dawn flank due to smaller magnetic field tension when compared to the dusk flank (Nykyri, 2013). Recent statistical studies using 6 years of THEMIS data illustrate that the fluctuations in ULF Pc4-Pc5 and Pc3 range, which characterize the frequency range of fluctuations generated by the KHI (Miura & Pritchett, 1982), are indeed more enhanced in the dawn flank (Dimmock, Nykyri, et al., 2016; Nykyri & Dimmock, 2016). There are also more Pc3 velocity fluctuations observed at the dawn flank magnetosheath (Dimmock, Nykyri, et al., 2016), which could seed the growth of KHI.

There are many secondary mechanisms associated with the KHI that can make plasma heating and transport more efficient on the dawnside magnetopause flank: Magnetic reconnection inside KH vortices has been proposed as a mechanism for transporting mass across the magnetopause and generating the cold-dense plasma sheet (Hasegawa et al., 2009; Nykyri & Otto, 2001; 2004; Nykyri et al., 2006; Taylor et al., 2008). More recently, magnetic reconnection associated with KHI has been observed by the Magnetospheric Multiscale spacecraft (Eriksson, Lavraud et al., 2016) including the coherent resolution of the electron diffusion region (Eriksson, Wilder et al., 2016). KH associated ion-beams observed during a reconnection interval may act as a driver for ion-scale waves (Nykyri et al., 2006), which may in turn heat the plasma.

KHI may also lead to the formation of kinetic Alfvén waves (KAWs) at the magnetopause via mode conversion from ultra-low frequency MHD surface waves (Johnson & Cheng, 1997; Johnson et al., 2001). KAWs have been attributed to ion heating and plasma transport across the magnetopause (Hasegawa & Mima, 1978; Johnson & Cheng, 1997; Johnson et al., 2001; Lee et al., 1994; Rezeau et al., 1989). Observations consistent with this phenomenon have been shown to transport significant energy into the magnetosphere at the Alfvén resonance location (Chaston et al., 2007). KAWs have also been shown to develop in regions associated with reconnection (Chaston et al., 2009; Gershman et al., 2016). A statistical study by Yao et al. (2011) showed a dawn-dusk asymmetry in the spectral energy densities of ion gyroradii scale electromagnetic waves that favored the dawnside over the duskside magnetopause. More recently, Wilder et al. (2016) showed observations of large-amplitude electrostatic waves in a turbulent mixed plasma associated with KHI.

Using measurements from two Cluster spacecraft ≈80 km apart, Moore et al. (2016) recently unambiguously identified, in terms of an observational dispersion relation, a fast magnetosonic (FMW) wave packet in the vicinity of a KH vortex. The wave energy associated with the FMW interval accounted for a substantial amount of energy transport to the cold-component ion population. It was suggested that velocity shears at the flank magnetopause generate KHI at the MHD scale, which contained sufficient kinetic energy to power ion-scale FMW generation in the vicinity of a rolled-up KH vortex. Shell-like ion distributions observed inside the KH vortex were suggested as a likely driving source of the observed FMW. During this event, also other wave packets were observed with properties consistent with KAWs in magnetosheath side of the vortex, as well as another wave packet in mixed region that had properties consistent with FMW. The ion-scale wave observations and associated heating during this event are consistent with cross-scale energy transport from fluid-scale KHI, into ion-scale waves, allowing the kinetic energy of the velocity shear to be transferred into heat energy of ions. We have calculated various wave properties such as ellipticity, Poynting flux, wave power, and wave propagation angle with respect to the magnetic field, during this event, which can be used as a benchmark for the interpretation of the results of this statistical study of the wave properties.

In the present study our motivation is to study (a) whether ion-scale waves are more abundant when KHI is present and (b) whether ion heating is more abundant during ion-scale wave observations when KHI is present compared to crossings without KHI. The presence and role of ion-scale turbulence during KHI is currently poorly understood; especially its impact on plasma transport at the magnetopause. The present study aims to shed light on this unresolved issue by comparing the statistics of (temporal) ion-scale wave properties and plasma parameters between boundary crossings during ≈12 h of KHI to crossings where signatures of active KHI are absent.

We have organized the manuscript as follows: (1) Methodology: an introduction into event selection (section 2.2), data binning (section 2.3), and the ion-scale wave interval algorithm (section 3.2); (2) Results: degree of polarization and magnetic compressibility over a broad range of frequencies (section 3.1), ion-scale wave properties with respect to propagation angle including total magnetic wave power (section 3.2.1), total integrated Poynting flux (section 3.2.2), electric field to magnetic field ratio (section 3.2.4), and plasma parameters (section 3.2.5); (3) Discussion; (4) Conclusions; and (5) Appendices A and B: solar wind effects on magnetosheath plasma properties and Doppler shift effects on ion-scale wave intervals.

2. Methodology

2.1. Data and Instrumentation

All magnetospheric data in this current work come from the Cluster satellite mission (Escoubet et al., 1997), composed of four spacecraft orbiting in a tetrahedral formation. Each of the four spacecraft is equipped with instrumentation to measure both electromagnetic fields and plasma moments. The plasma moments and ion energy spectrograms are provided by the Cluster Ion Spectrometer (Rème et al., 1997). The Fluxgate Magnetometer instrument provides the high-resolution magnetic field measurements at a 22.4 Hz sampling rate (Balogh et al., 1997). The electric field data were collected by the Electric Fields and Waves experiment (EFW) (Gustafsson et al., 1997), which is part of the wave consortium controlled by the Digital Wave Processor (Woolliscroft et al., 1997).

2.2. Event Selection

The KHI database was populated from a list of previously published KH events, confirmed with simulations, with varying IMF configurations. This database contains five dawn-flank events—one mixed PS-OPS (Otho-Parker Spiral) IMF event (Nykyri et al., 2006), two PS IMF events (Moore, 2012; Moore et al., 2016), and two OPS IMF events (Moore, 2012; Moore et al., 2016)—and one dusk flank event under northward IMF (Hasegawa et al., 2004). Differences in events across the solar phases are not taken into consideration for the following event selection as the effect of solar phase on KHI is beyond the scope of this paper. Observations consistent with KHI are quasi-periodic variations in the plasma and field parameters including anticorrelated density and temperature, bipolar variation of the magnetic field component normal to the magnetopause, and total pressure variations, with strong pressure minimums at the center of the vortex. These observations are depicted in an overview plot of the KHI event from 6 June 2002 (Moore, 2012; Moore et al., 2016), shown in Figure 1.

For the non-KHI database, the Cluster Science Archive was searched for boundary crossing that did not exhibit the criteria for KHI. It is worth noting that although the non-KHI database consists of events that lack observations consistent with KHI, there is currently no way to exclude the possibility that KHI was previously acting on the magnetopause boundary. However, since the motivation is to study the in situ effects of KHI and ion-scale wave properties, previous effects on the boundary are ignored.

The total time duration of observations is about ≈12.5 h for KH events and ≈12.5 h for non-KH events. Any discrepancies in time are taken into account in the various statistics by including a weighting factor.

2.3. Data Binning

In order to perform statistics on boundary crossings during KHI activity, the data are binned with respect to ion energy level. Due to the rolled-up magnetopause boundary produced by the KHI, spacecraft have periodic encounters with magnetospheric-like and magnetosheath-like plasma populations. This results in spatial variations in ion energies between cold component (magnetosheath-like) and hot component (magnetospheric-like) as well as a mixed energy population during periods of KHI (Hasegawa et al., 2004). Thus, ion energies are separated into three levels—magnetosphere (MSP), magnetosheath (MSH), and mixed (MIX) levels—representative of their corresponding plasma regions. Determination of these energy level values (and subsequent plasma region bin) is based on statistical analysis of the ion distributions in flux-energy space over an event interval and is performed systematically for each event. The ion energy spectrogram data

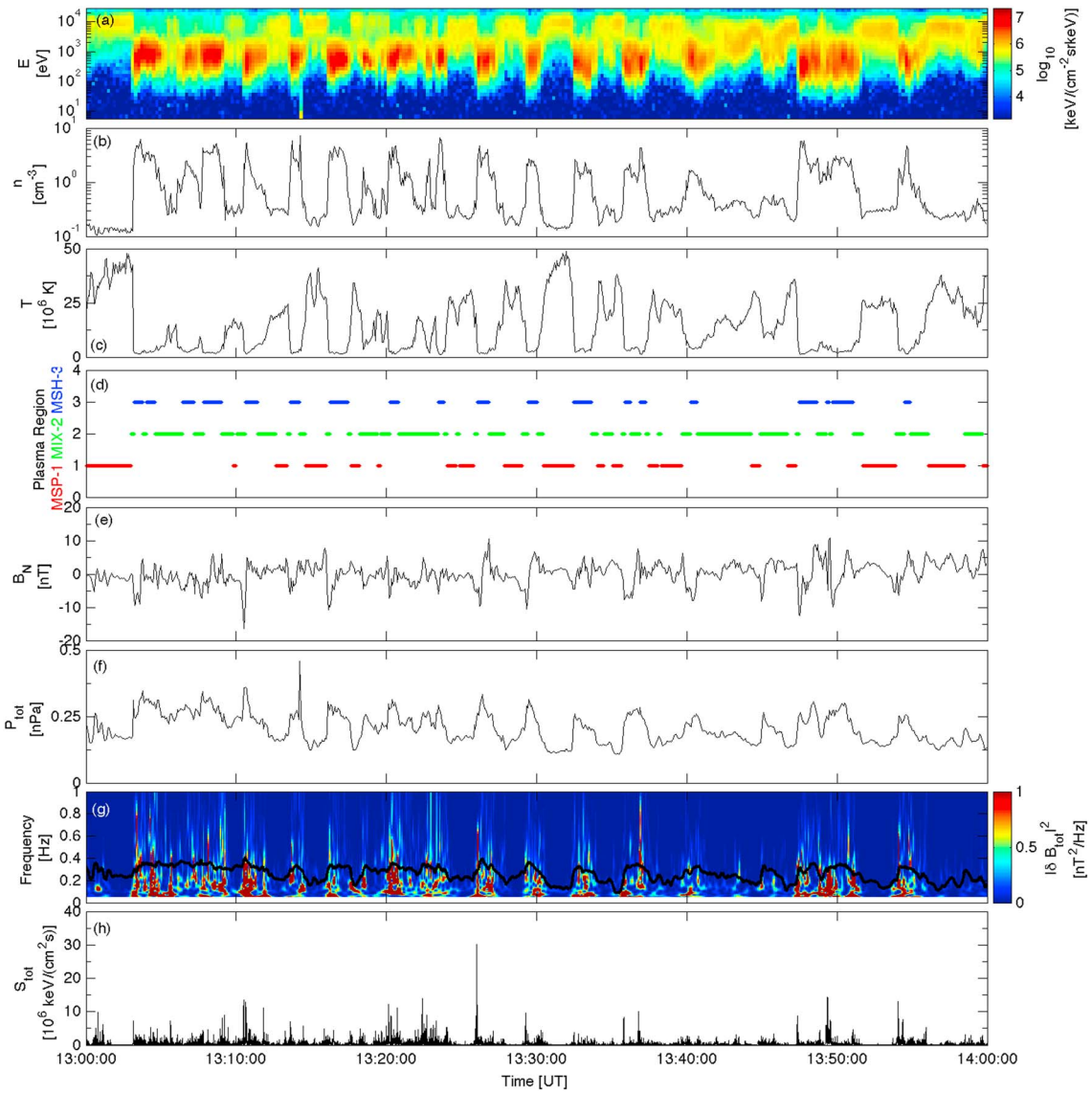

Figure 1. Overview plot of 6 June 2002 KHI event during PS IMF including the omnidirectional (a) ion energy spectrogram, (b) ion number density n, (c) ion temperature T, (d) plasma region, (e) normal component of the magnetic field B_N, (f) total pressure, (g) total magnetic wave power $|\delta B_{tot}|^2$, and (h) total Poynting flux S_{tot}.

from the Hot Ion Analyzer (HIA) on board Cluster spacecrafts 1 and 3 have been obtained from the Cluster Science Archive (Laakso et al., 2010).

Ion energy thresholds for the magnetospheric (MSP) and magnetosheath (MSH) plasma populations are determined by analyzing peaks in the ion energy histograms. The mixed (MIX) threshold is determined as a log average of the MSP and MSH thresholds. For example, Figure 2 depicts how the MSP and MSH energy thresholds are determined from the omnidirectional ion energy spectrograms. Initially, the ion-energy corresponding to the max energy flux is recorded for each time step—the energy-flux distributions are shown for each time step in Figure 2a and a qualitative plot in energy flux space is depicted in Figure 2b. After each ion energy at each time step has been recorded for a single event, counts are tallied to calculate a histogram in energy space—the ion energy histogram is plotted in Figure 2c. The thresholds for the MSP, MIX, and MSH plasmas compiled from the 6 June 2002 event were determined to be approximately 722, 2,670, and 9,900 eV, respectively. Data are then binned in the MSP, MIX, and MSH according to which ion energy threshold the (flux) weighted average energy—calculated at each time step from the ion energy spectrogram—is in closest proximity to (on the $\log_{10}$-scale). Results for the binning algorithm for 6 June 2002 KHI event are displayed in Figure 1d.

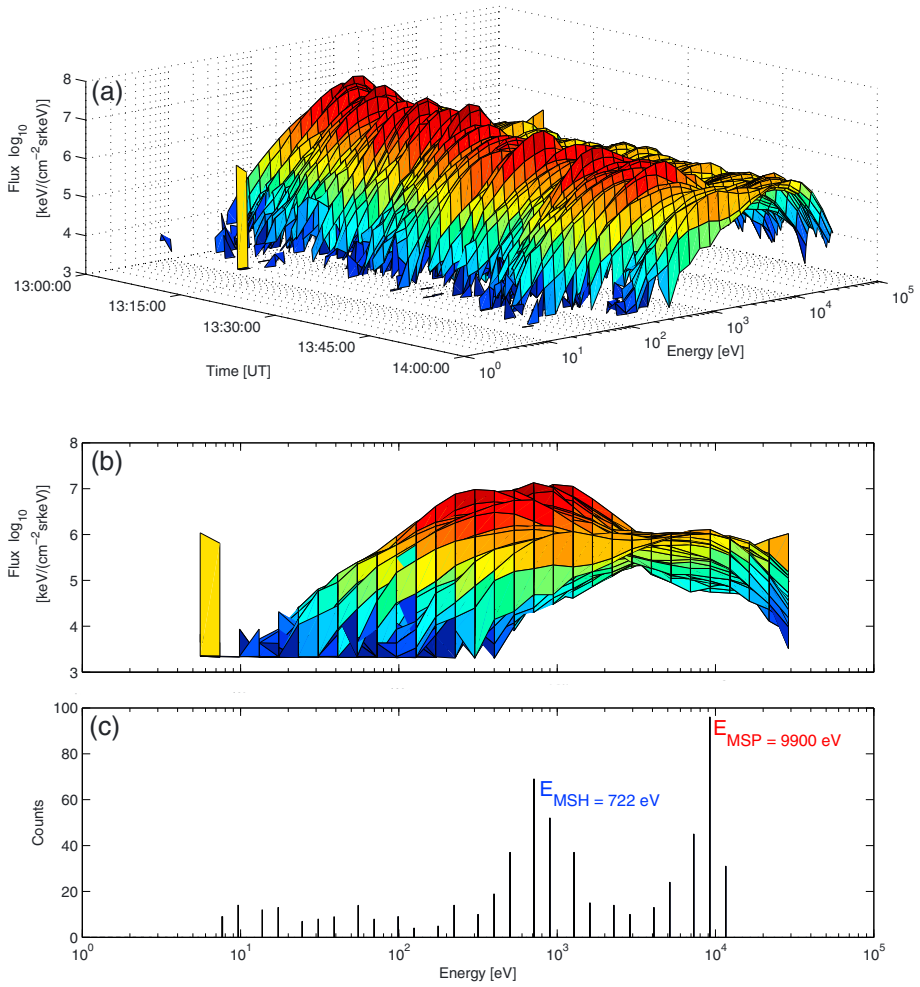

Figure 2. Overview of statistical determination of plasma energy threshold levels from 6 June 2002 KHI event including the (a) omnidirectional ion energy spectrogram, (b) the omnidirectional ion energy spectrogram in energy flux space, and the (c) omnidirectional ion energy histogram.

This process is repeated independently for each event. Statistics on the kinetic wave properties are then compiled for the collection of KHI and non-KHI events. Note that for the boundary crossings without KHI, there also exists these three distinct energy regions. It is possible that the mixed layer during the non-KH events that characterizes the LLBL population has been previously produced by the KHI, so it is difficult to fully avoid contamination from previous processes and compare boundary layer properties with and without KHI. However, we argue that the ion-scale wave packets driven by the active KHI are short lived due to efficient damping (Moore et al., 2016), so it is feasible to assume that the ion-scale wave amplitudes would be larger when the active source is present.

2.4. Minimum Variance Analysis of Broadband and Ion-Scale Wave Intervals

In order to collect information on the propagation angle θ_{kB} between the wave (unit) vector $\hat{k}$ and the background magnetic field **B**, a sliding window using minimum variance analysis (MVAB) on the high-pass filtered magnetic field is performed (Sonnerup & Scheible, 1998). A 0.005 Hz cutoff frequency high-pass filter is used to remove low-frequency oscillations associated with the KH waves. The (temporal) length of the window Δt is proportional to the desired frequency such that $\Delta t = 1/(2f_j)$ where j is the jth index of the frequency array. A step size equal to 50% of Δt is used allowing for some overlap. The frequency array is a power of 2 distribution of frequencies ranging from 0.005 Hz to 2.7 Hz. The lower bound of this frequency range was chosen to filter out the low-frequency oscillations from the KHI as mentioned previously. The higher limit of the frequency band was chosen based on the Moore et al. (2016) observations of a FMW that was shown to have a frequency range of approximately 9 times the ion cyclotron frequency. We perform statistical analysis

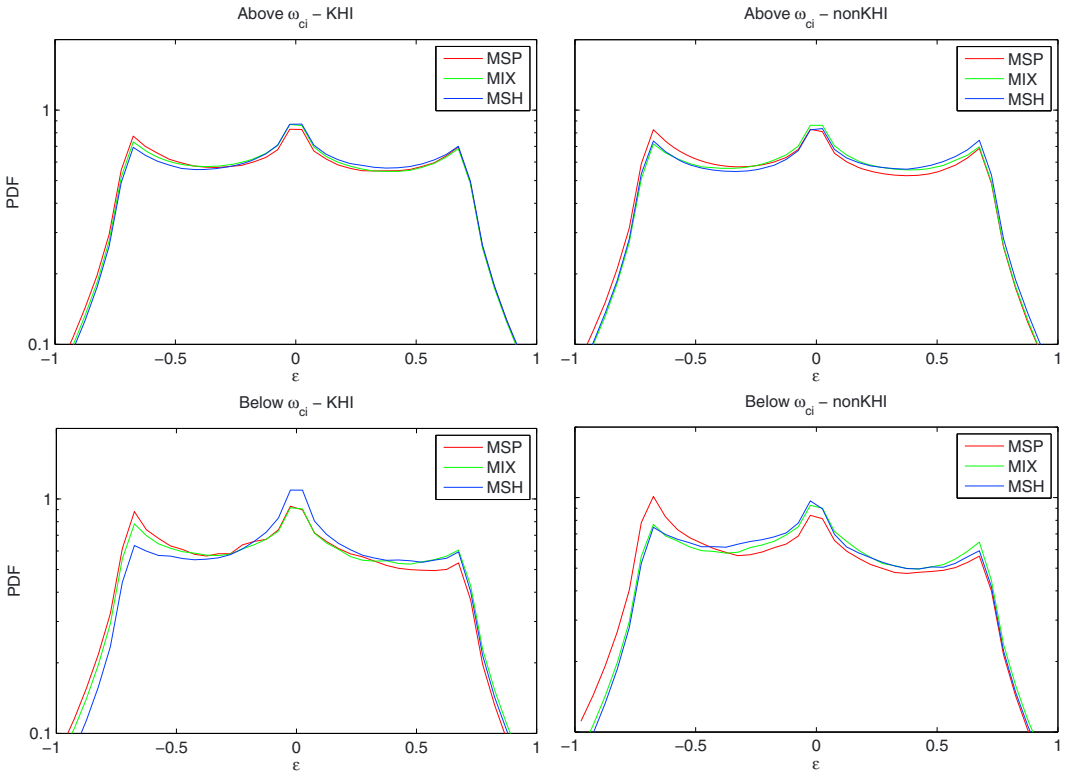

Figure 3. Degree of polarization ϵ calculated in the MSP (red), MIX (green), and MSH (blue) plasma (top row) above and (bottom row) below the local ion cyclotron frequency f_{ic} during (left column) KHI and (right column) non-KHI events.

of magnetic field fluctuations both for broadband frequency range and for a narrower range close to local ion gyrofrequency, averaged over the plasma bin interval. For data integrity only MVAB wave intervals with an eigenvalue ratio $\lambda_{int}/\lambda_{min} > 5$ are retained. Furthermore, only well-polarized MVAB wave intervals ($\sqrt{\lambda_{int}/\lambda_{max}} > 0.5$) are retained for computing statistics.

3. Results

3.1. Broadband Statistics

The following broadband statistics are taken over a relatively large band of frequencies 0.005 Hz $\leq f \leq$ 2.7 Hz to offer a general account for the degree of polarization and magnetic compressibility over the three plasma regimes during KHI and non-KHI boundary crossings.

3.1.1. Degree of Polarization

The degree of polarization ϵ, plotted in Figure 3, is calculated from the Stokes' parameters compiled from the magnetic wave fields described by Carozzi et al. (2001). Probability distributions in ϵ are nonzero between approximately $\pm$0.9 for frequency ranges above (Figure 3, top row) and below (Figure 3, bottom row) the local ion cyclotron frequency f_{ic}. These distributions form a trident distribution containing three distinct peaks at approximately $\pm$0.675 and 0 for all plasma regimes at all frequencies. Overall, there is little distinction in the observed ϵ between KHI and non-KHI events. Furthermore, due to possible Doppler effects, an accurate weight of handedness (right hand versus left hand) in the plasma frame is not attainable.

3.1.2. Magnetic Compressibility

One-dimensional probability distribution functions depicting the magnetic compressibility $P_{B_{||}}/P_{B_{\perp}}$, where $P_{B_{||}}$ is the compressional magnetic wave power and $P_{B_{\perp}}$ is the magnetic wave power, are shown for the MSP, MIX, and MSH plasma regimes in Figure 4 for both KHI events (left) and non-KHI events (right). Although statistically transverse ($P_{B_{||}}/P_{B_{\perp}} < 1$) for all plasma regimes, the wave observations become more compressive when moving from the MSH to MIX to MSP plasma (see Figure 4, left). Because KHI has been associated with mode conversion at the magnetopause (Chaston et al., 2007; Johnson & Cheng, 1997; Johnson et al., 2001), one would expect to see an amplification in the transverse wave power in the vicinity of the magnetopause

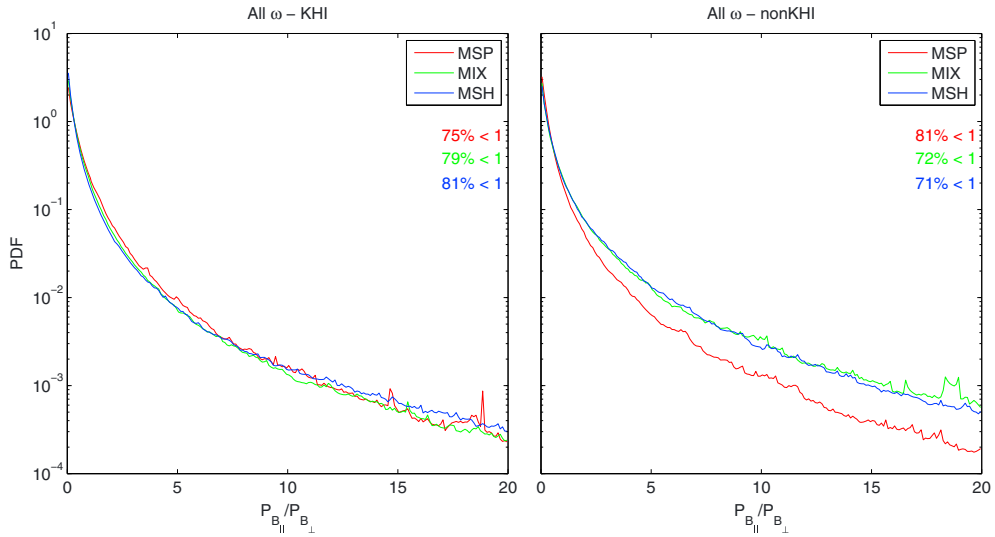

Figure 4. Magnetic compressibility $P_{B_{||}}/P_{B_{\perp}}$ calculated in the MSP (red), MIX (green), and MSH (blue) plasma for all frequencies (0.05 Hz $\leq f \leq$ 2.7 Hz) during (left) KHI and (right) non-KHI events.

(Johnson et al., 2001). To the contrary, this amplification in transverse wave power from the MSH to MIX to MSP is a feature presented in the non-KH events (see Figure 4, right). It is expected that this feature is missed in the KH events due in part by the reflection of KAWs at the Alfvén resonance location (Johnson et al., 2001) back into the MSH.

3.2. Ion-Scale Wave Intervals

The statistics for the ion-scale wave intervals are obtained by considering frequency bins near the local ion cyclotron frequency. Because the ion cyclotron frequency is an averaged value, frequencies in close proximity above and below are considered, centered at f_{ic}. From the frequency array detailed in section 3.2, the frequency range of the ion-scale wave intervals includes $[f_{(j_{ic}-10)}, f_{(j_{ic}+10)}]$, where j_{ic} is the index of the frequency bin corresponding to the local ion cyclotron frequency. The 2-D histograms consisting of θ_{kB} and kinetic wave properties are compiled by tallying counts accrued in each parameters' overlapping bins.

All of the ion-scale wave properties are calculated in the spacecraft frame. Because it is not possible to account for the actual Doppler shift for each of the MVAB wave intervals on a statistical basis, we approximate

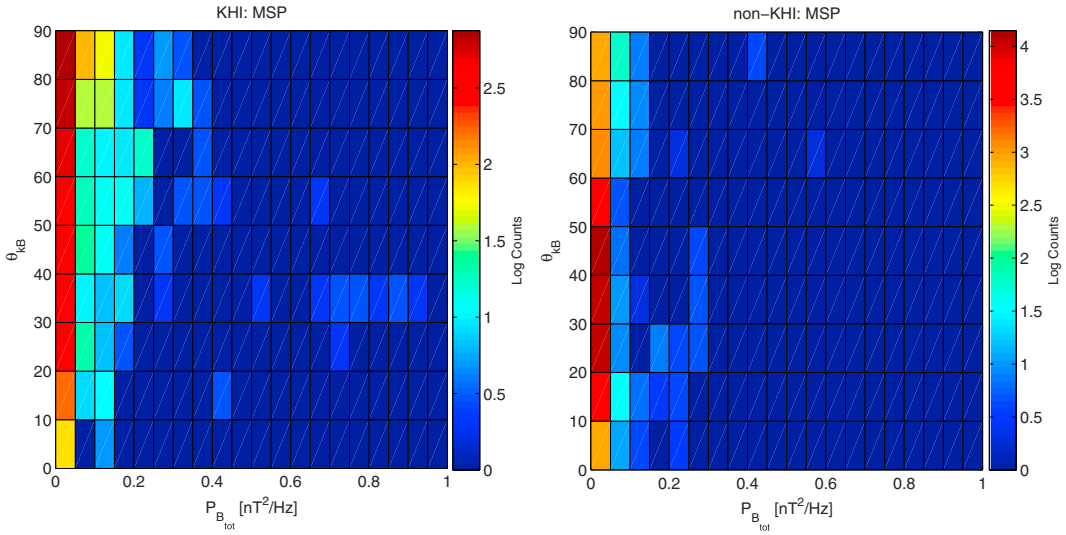

Figure 5. The 2-D distributions of mean total magnetic wave power versus wave propagation angle (P_{tot} versus θ_{kB}) between (left) KHI and (right) non-KHI events in the MSP plasma regime.

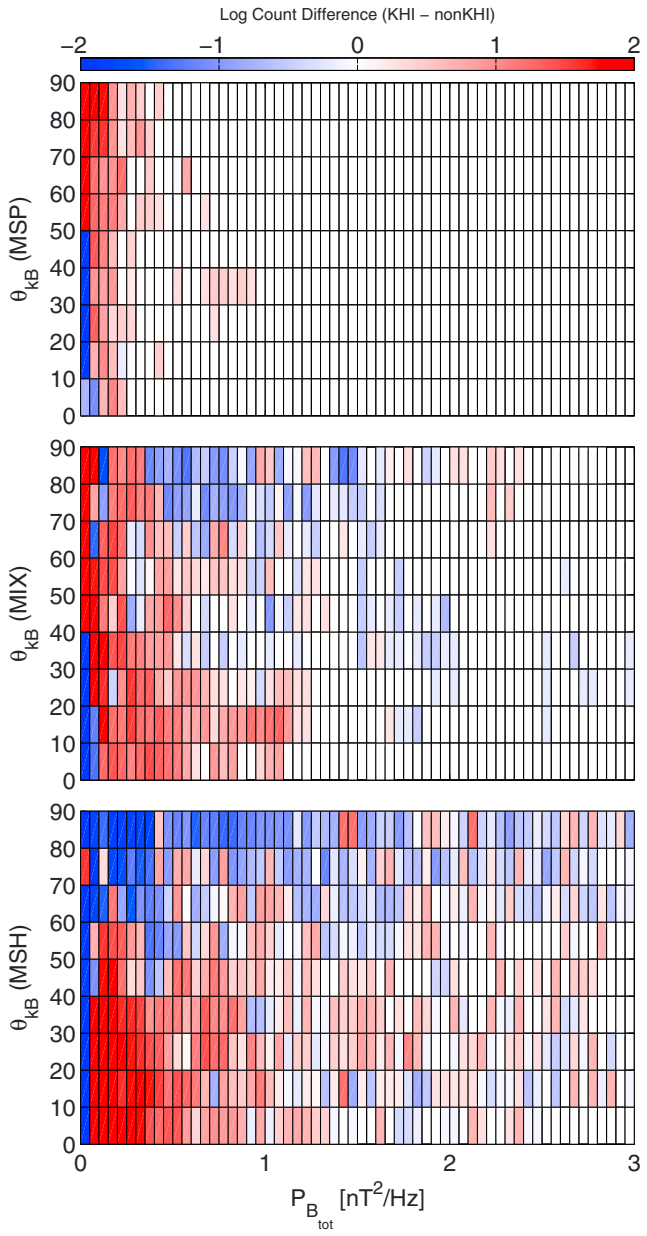

Figure 6. The 2-D comparative distributions of mean total power (P_{tot}) versus propagation angle (θ_{kB}) between KHI and non-KHI events. (top) MSP, (middle) MIX, and (bottom) MSH plasma regimes.

the possible effects by assuming specific wave modes. For a brief analysis on the Doppler shift effects, please refer to Appendix B.

The MVAB (ion-scale) parameters including the MVAB specific entropy $\mathcal{S}_{MVAB}$, the MVAB plasma beta β_{MVAB}, magnetic wave power P_{tot}, and the scaled E/B ratio $\mathcal{P}$ are averaged over each MVAB wave interval in the f_{ic} frequency range. The total integrated Poynting flux S_{int} is integrated over each MVAB wave interval in the f_{ic} frequency range. The raw parameters such as the raw specific entropy $\mathcal{S}_{raw}$ and raw plasma beta β_{raw} are calculated at each time step from the unprocessed time series data and are not filtered by temporal scale.

3.2.1. Mean Total Magnetic Wave Power, P_{tot}

The mean total magnetic wave power, $P_{tot} = \overline{|\delta B_{tot}|^2}$, is determined by taking the mean of the total magnetic wave power over each MVAB wave interval. The 2-D distribution of P_{tot} versus wave propagation angle, θ_{kB}, for the MSP plasma regime are shown in Figure 5 (left) (KHI events) and Figure 5 (right) (non-KHI events). From Figure 5 (left), a higher count density ($\log_{10}$ counts per cell) during KHI events is observed for obliquely propagating waves with relatively low power (P_{tot}), with the highest count density accounted for in the 80°–90° bin. A more moderate count density is observed for oblique waves (50°–90°) with significantly higher power for KH events than for non-KHI events. In contrast, during non-KHI events the highest count density is observed for 20°–50° propagating, low power waves (see Figure 5, right).

To offer a better comparative analysis between statistics gathered during KHI and non-KHI events, a $\log_{10}$ count difference between the KHI and non-KHI events is calculated for each of the kinetic wave properties and plotted in the following 2-D distributions. Difference distributions in which observations taken from KHI events dominate are designated by red, whereas those dominated by observations taken from non-KHI events are designated by blue, and a zero $\log_{10}$ count difference is designated by white. Please note that an actual count difference of 0 or 1 is assigned a $\log_{10}$ count difference of 0.

The 2-D comparative distributions of the mean total wave power versus propagation angle (P_{tot} versus θ_{kB}) depicting the $\log_{10}$ count difference between observations made during KHI and non-KHI events are shown in Figure 6 for the MSP, MIX, and MSH plasma regimes, respectively. In the MSP plasma regime plotted in Figure 6 (top), more obliquely propagating waves between 50° and 90° are observed during KHI events for a broad range of power ($P_{tot} \approx 0$–0.9 nT^2/ Hz), whereas during non-KHI events more waves with low power ($P_{tot} \approx 0$–0.1 nT^2/Hz) and lower propagation angle ($\theta_{kB} \approx 0°$–$50°$) are observed. A similar trend is seen for waves with low power ($P_{tot} \approx 0$–0.1 nT^2/Hz) in the MIX plasma regime, where observations of obliquely propagating waves ($\theta_{kB} \approx 40°$–$90°$) are dominant during KHI events and waves with lower propagation angle ($\theta_{kB} \approx 0°$–$40°$) are dominant during non-KHI events (see Figure 6, middle). There is a larger disparity between high power waves in the MIX plasma regime when compared to the MSP, with a slight preference in the KHI event observations between $\theta_{kB} = 40°$ and 70°. The quasi-perpendicular propagating ($\theta_{kB} = 70°$–$90°$) observations tend to be more non-KHI dominant for $P_{tot} > 0.35$ nT^2/Hz. In the MSH plasma regime as shown in Figure 6 (bottom), the low power wave observations are non-KHI dominant for $0° < \theta_{kB} < 70°$ and $80° < \theta_{kB} < 90°$. There is a slight asymmetry for waves contributing to the higher power with a clear dominance in the KHI events for low propagation angles ($\theta_{kB} \approx 0°$–$30°$).

3.2.2. Total Integrated Poynting Flux

The Poynting flux and the wave electric to magnetic field ratio are calculated from the wave electric and magnetic fields provided by the wavelet transform of the high-resolution electric and magnetic fields. Because Cluster's EFW instrument can only resolve the 2-D electric field in the spin plane, the third component

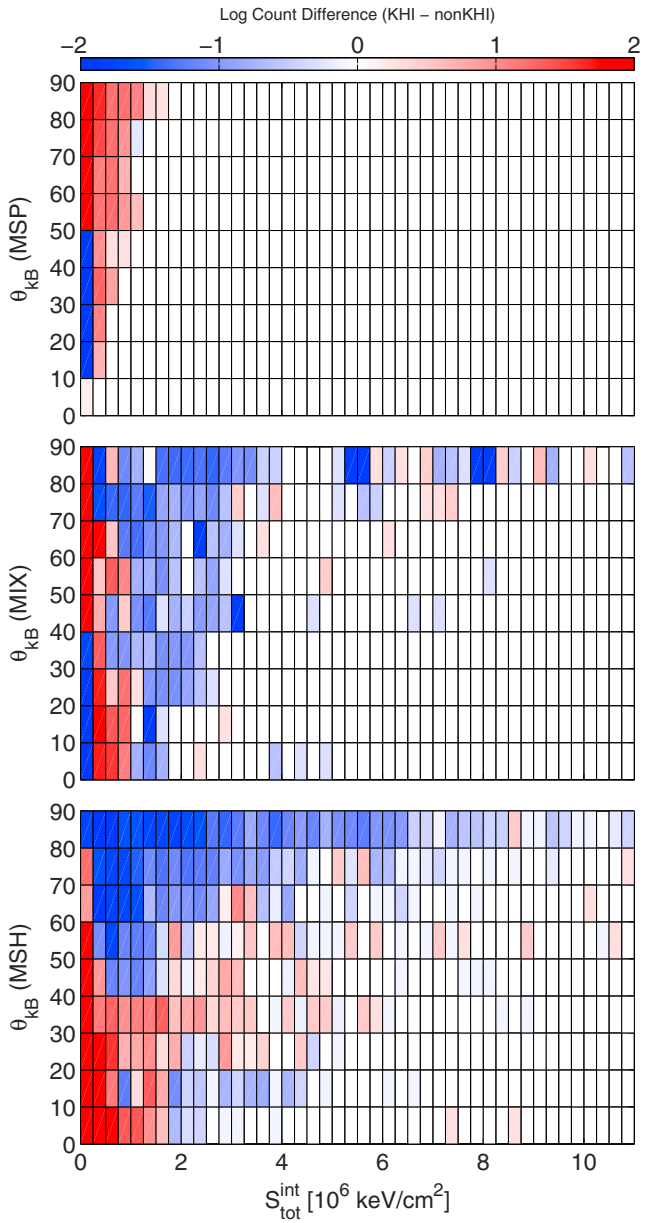

Figure 7. The 2-D comparative distribution of the integrated Poynting flux versus propagation angle (S_{int} versus θ_{kB}). (top) The MSP, (middle) MIX, and (bottom) MSH plasma regimes.

is calculated based upon the assumption that $\mathbf{E} \cdot \mathbf{B} = 0$. The total integrated Poynting flux, $S_{int} = \int S_{tot} \partial t$, associated with the FMW interval from Moore et al. (2016) is approximately 4.4×10^6 keVcm^{-2}. For the statistics S_{int} is computed by integrating the wave Poynting flux over each MVAB wave interval. The 2-D distributions of S_{int} versus θ_{kB} are displayed in Figure 7. In Figure 7 (top), observations made in the MSP plasma regime show a broad distribution of KHI dominant S_{int} for obliquely propagating waves ($\theta_{kB} = 50°-90°$) and non-KHI dominant (narrowly distributed S_{int}) wave observations for lower propagation angles ($\theta_{kB} = 10°-50°$). In the MIX plasma regime plotted in Figure 7, however, the KHI dominant observations are subdued to a narrow band of low S_{int} for $\theta_{kB} \approx 40°-90°$. The non-KHI dominant wave observations comprise a narrow band of S_{int} for lower propagating angles ($\theta_{kB} \approx 0°-40°$). There tends to be more non-KHI dominant wave observations of higher S_{int}, the more oblique the propagation angle becomes. There is a transition to non-KHI dominant wave observations in MSH plasma regime as seen in Figure 7 (bottom) for the entire range of S_{int}. Overall, there is a slight asymmetry for moderate integrated Poynting flux ($S_{int} > 0.2510^6$ keVcm^{-2}) where obliquely propagating waves ($\theta_{kB} = 40°-90°$) are non-KHI dominant and waves with smaller propagation angles ($\theta_{kB} = 0°-40°$) are dominant during KH events.

3.2.3. Wave Electric to Magnetic Field Ratio Dispersion: FMW

Moore et al. (2016) showed unambiguous observations of a quasi-perpendicular propagating ($\theta_{kB} \approx 85°, 88°$) FMWs observed close to center of a KH vortex (evidenced by a total pressure minimum) with sufficient energy to account for observed ion heating. The wave electric to magnetic field ratio (scaled by the local Alfvén speed), $(|\delta E_\perp|/|\delta B_\perp|)/v_A$, versus the wave frequency calculated during this FMW interval is plotted in Figure 8. For $f < f_{ic}$, where $f_{ic} \approx 0.3$ Hz, there is a strong count density between approximately 0–4, indicating the waves are mostly electromagnetic. This distribution broadens (electrostatic component increases) for $f > f_{ic}$, but the strongest count densities are still in electromagnetic regime 0–10.

Because the local f_{ic} for the FMW interval is approximately 0.3 Hz, the frequency range of interest in context to the MVAB wave interval statistics is approximately 0.20–0.45 Hz. In Figure 8 $(|\delta E_\perp|/|\delta B_\perp|)/v_A$ is approximately 0–4 for the strongest count densities and up to 8 for the lower count densities.

3.2.4. Mean $\delta E/\delta B$ Ratio Distribution

$\mathcal{P}$ is calculated by taking the mean $(|\delta E_\perp|/|\delta B_\perp|)/v_A$ over each MVAB wave interval in close vicinity to f_{ic} ($[f_{(j_{ic}-10)}, f_{(j_{ic}+10)}]$). The 2-D distribution of $\mathcal{P}$ versus the propagation angle is plotted in Figures 9 (top) to 9 (bottom). In the MSP plasma regime (Figure 9, top), the distribution of $\mathcal{P}$ versus θ_{kB} shows a dominance for KH events across all values of $\mathcal{P}$ for the obliquely propagating waves ($\theta_{kB} = 40°-90°$). This KH-dominant distribution is much narrower ($\mathcal{P} \approx 0.25-3$) for smaller propagation angles ($\theta_{kB} = 0°-40°$). One interesting feature in the MSP plasma is the non-KH-dominant wave observations consisting of $3 < \mathcal{P} < 40$ and $10° < \theta_{kB} < 50°$. The $\mathcal{P}$ versus θ_{kB} distribution for the MIX plasma regime reveals KH-dominant wave observations for oblique propagation angles and non-KH dominant for lower propagation angles (see Figure 9, middle). Additionally, the wave observations are non-KH dominant for nearly all propagation angles for $\mathcal{P} > 10$.

Observations in the MSH plasma regime (Figure 9, bottom) show a narrow KHI dominant distribution in $\mathcal{P}$ ($\approx 0.25-2$) for all θ_{kB}, whereas wave observations at higher values of $\mathcal{P}$ are non-KHI dominant for all θ_{kB}.

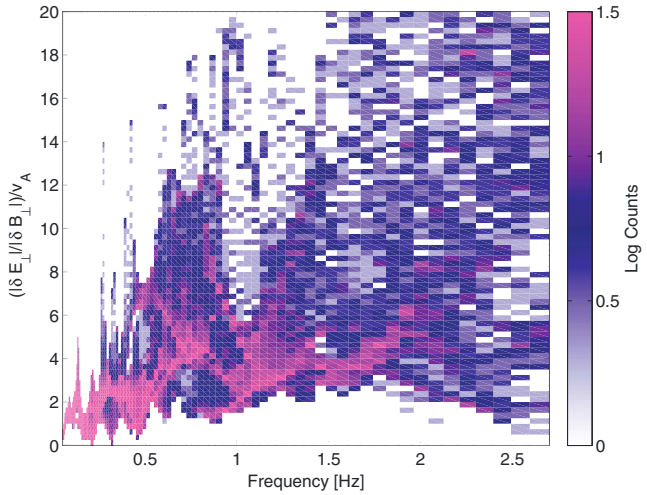

Figure 8. Scaled wave electric to magnetic field ratio $(|\delta E_{\perp}|/|\delta B_{\perp}|)/v_A$ from 6 June 2002 FMW interval.

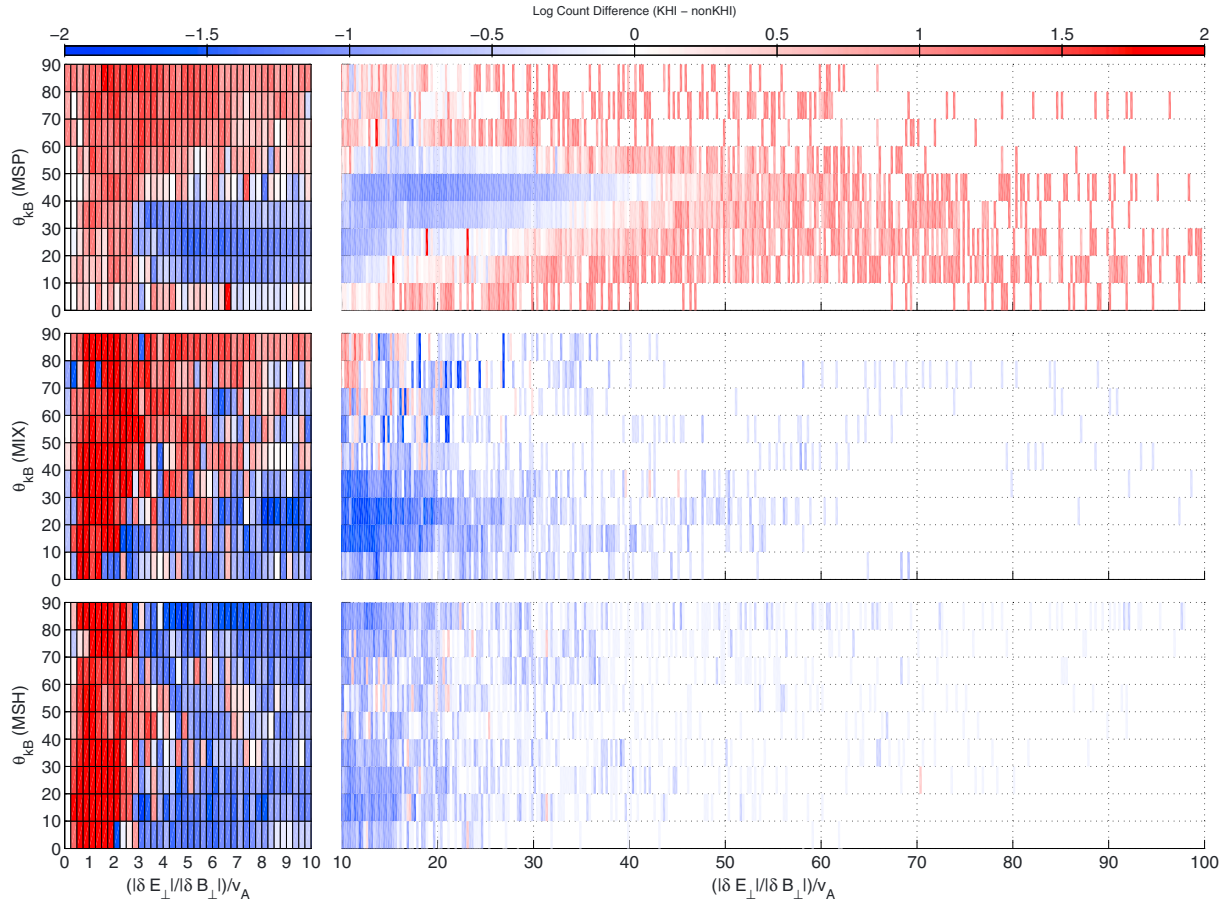

Figure 9. The 2-D comparative distributions of scaled mean electric to magnetic field ratio versus propagation angle. (top) MSP, (middle) MIX, and (bottom) MSH plasma regimes.

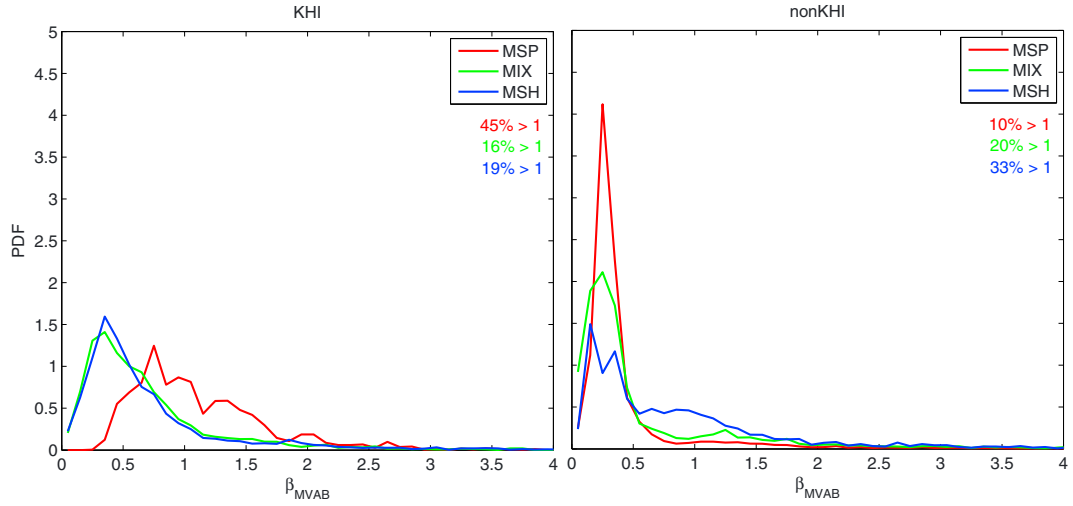

Figure 10. Plasma beta calculated during the ion-scale MVAB wave intervals for the MSP (red), MIX (green), and MSH (blue) plasma for the (left) KH and (right) non-KH events.

The broad KHI dominant distributions in $\mathcal{P}$ at oblique θ_{kB} (50°–90°) for the MSP and MIX plasma regimes are consistent with the FMW $\delta E/\delta B$ ratio shown in Figure 8 in the vicinity of the f_{ic}. It is well known that $\mathcal{P} \geq 1$ for KAWs (Chaston et al., 2007; Chaston et al., 2012; Stasiewicz et al., 2000).

3.2.5. Plasma Parameters

In this section, plasma parameters are shown for both the ion-scale wave intervals and from the raw data. Please refer to Appendix A for an analysis on possible solar wind effects on magnetosheath plasma parameters. The plasma beta β calculated over the MVAB wave intervals is plotted in Figures 10 (left and right). During the KHI events the β_{MVAB} probability distributions in the MIX and MSH plasma regimes are offset with peaks <1 compared to that in the MSP plasma as seen in Figure 10 (left). When integrating the tails of the distributions in the MIX and MSH plasma, only ≈16% and 19% (respectively) of all the wave intervals have $\beta_{MVAB} > 1$. For KHI events ≈45% of all wave intervals in MSP plasma regime have $\beta_{MVAB} > 1$. During the non-KHI events, the distributions in all three plasma regimes share similar peaks, with the broadest distribution in the MSH plasma (Figure 10, right). Integrating the tails of the distributions reveals that the β_{MVAB} steadily increases from the MSP (≈10% > 1) to the MIX (≈20% > 1) to the MSH (≈33% > 1) plasma regime. It is interesting to note that in these β_{raw} distributions calculated from the non-KH events share approximately the same peaks.

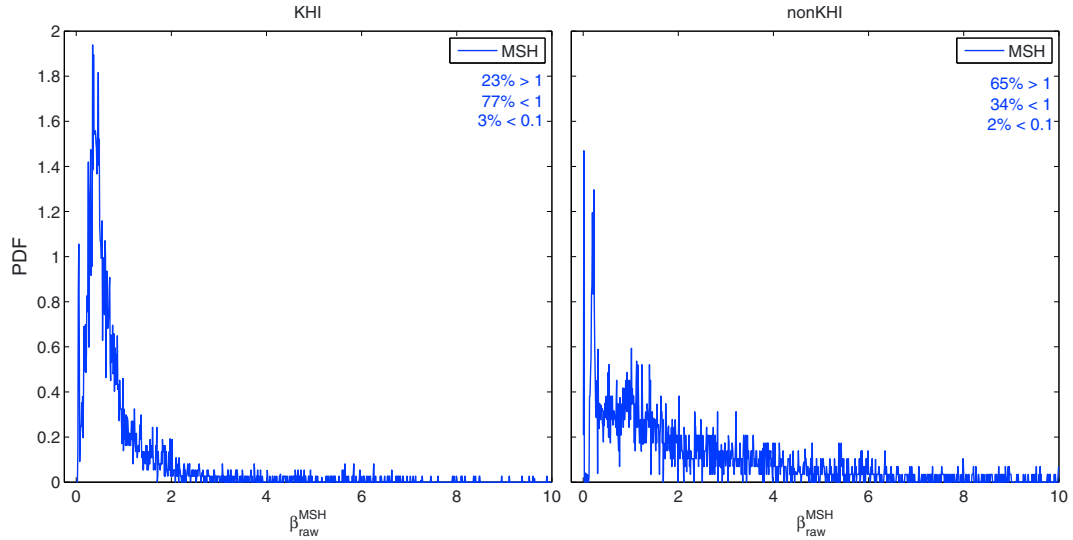

Figure 11. Raw plasma beta calculated for the MSH plasma for the (left) KH and (right) non-KH events.

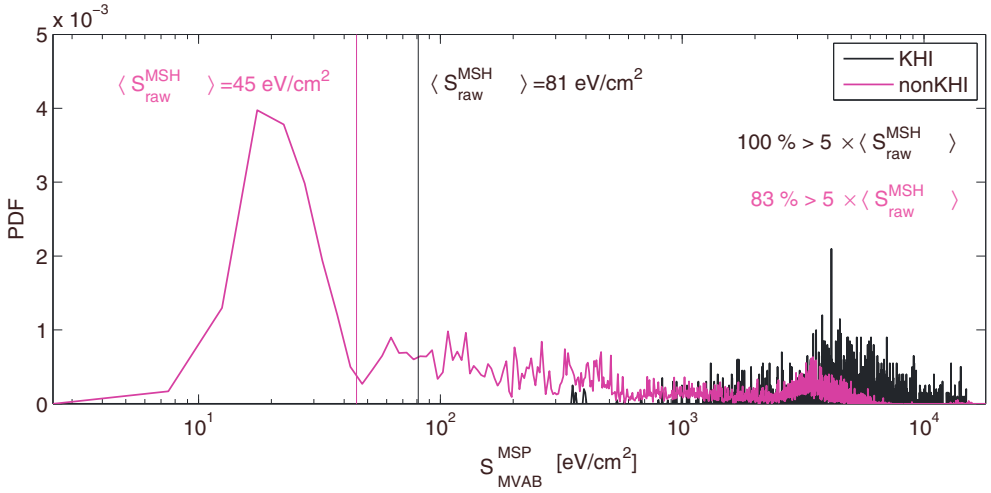

Figure 12. (left and right) Specific entropy calculated during the ion-scale MVAB wave intervals in the MSP plasma for the KH (black line) and non-KH events (magenta line). The log-mean average of the raw MSH specific entropies are displayed for the KH and non-KH events by the vertical black and magenta lines, respectively.

Although the probability distribution functions (PDFs)—calculated from their respective histograms—from Figure 10 (left and right) depict ion-scale waves propagating through lower beta MSH plasmas during KH events compared to the non-KH events, it is worthwhile to inspect the raw plasma beta β_{raw}^{MSH} observed in the MSH plasma regime. Figure 11 (left and right) shows the 1-D distributions of the raw MSH plasma beta calculated over the range $0 < \beta \leq 10$ for the KH and non-KH events, respectively. It should be noted that the raw MSH data value range extends beyond β_{raw}^{MSH}; however, the low MSH β (relative to 1) is of special interest. Hall MHD simulations of the dayside magnetopause have shown that a significant specific entropy increase from the inflow to outflow region, associated with magnetic reconnection, is only possible for sufficiently low plasma beta ($\beta << 1$) in the inflow region (Ma & Otto, 2014). Although there exists components of the β_{raw}^{MSH} PDFs from both the KH and non-KH events that are much lower than one, they are statistically insignificant–≈3% and 2% of the PDFs have a raw MSH plasma beta less than 0.1 for the KH and non-KH events, respectively. Ma and Otto (2014) concluded that $\beta \approx 0.1-1$ in the magnetosheath is insufficient for a specific entropy increase of 1 to 2 orders of magnitude due to magnetic reconnection. From Figure 11, β_{raw}^{MSH} is lower during the KH events compared to the non-KH events—≈77% < 1 and ≈34% < 1 for the KH and non-KH events, respectively.

When calculating the mean specific entropy over the MVAB wave intervals (S_{MVAB}), there is a significantly larger increase in the specific entropy (indicative of strong nonadiabatic heating) during the KHI events (Figure 12 (left and right)). Careful analysis was performed on the tails of the distributions from the MSP plasma regime relative to the log-mean average of the raw MSH specific entropy $\langle S_{raw}^{MSH} \rangle$ (please see Table 1). During the KH events, all of the specific entropy in the MSP plasma revealed an increase of at least 5 times that of the raw log-mean average specific entropy in the MSH, while during non-KHI events only ≈83% showed

Table 1
Details on the Raw Specific Entropy Across the MSP, MIX, and MSH Plasma Regimes

	n	$\langle S_{raw}^{n} \rangle$	$\langle S_{MVAB}^{n} \rangle$	P_{raw}^{n} [a]	P_{MVAB}^{n} [b]	$\frac{\langle S_{raw}^{n} \rangle}{\langle S_{raw}^{MSH} \rangle}$
KHI	MSP	4.87×10^3	4.59×10^3	100%	100%	60
	MIX	1.27×10^3	1.03×10^3	82%	78%	16
	MSH	80.6	83.5	9%	9.2%	1
non-KHI	MSP	2.89×10^3	1.10×10^3	100%	83%	59
	MIX	754	771	81%	77%	15
	MSH	45.4	141	35%	35%	1

[a] P_{raw} = % raw data points greater than $5 \times \langle S_{raw}^{MSH} \rangle$. [b] P_{MVAB} = integral of S_{MVAB}^{n} greater than $5 \times \langle S_{raw}^{MSH} \rangle$.

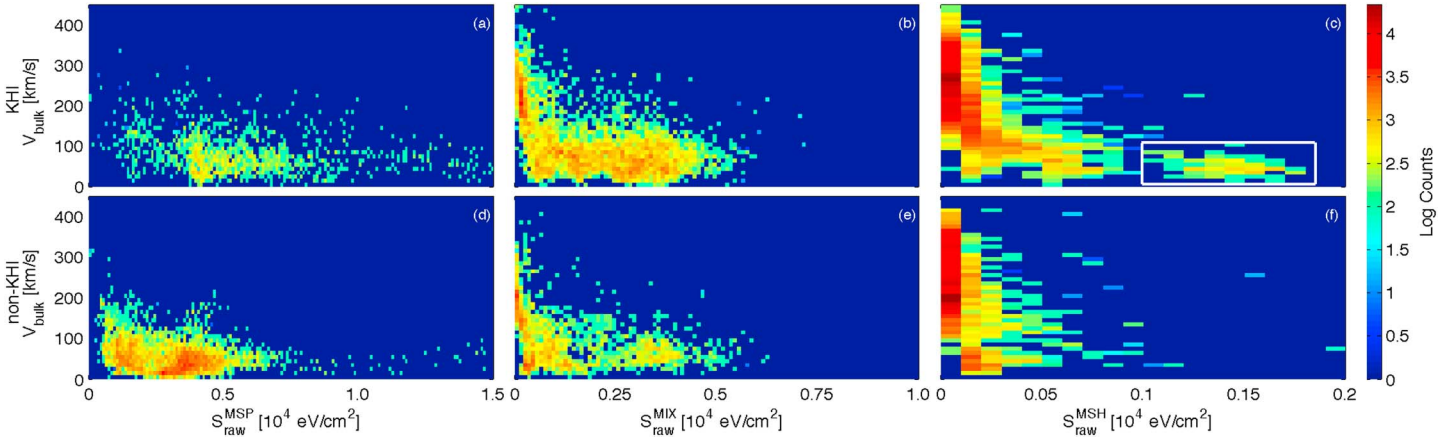

Figure 13. The 2-D distributions of bulk plasma velocity V_{bulk} versus raw specific entropy $\langle S^n_{raw} \rangle$ for the (a–c) KH and (d–f) non-KH events.

an increase by at least a factor of 5. This significant increase in the specific entropy from the MSH to MSP plasmas observed during the ion-scale wave intervals suggests strong nonadiabatic heating. When considering only the cold component ions, ionospheric data from the Defense Meteorological Satellite Program mapped into the plasma sheet suggest that the specific entropy may only increase by a factor of 5 (Johnson & Wing, 2009).

Figures 13a–13f show the raw specific entropy $\mathcal{S}_{raw}$ with respect to the bulk plasma flow (V_{bulk}) during the KH and non-KH events, respectively. $\mathcal{S}_{raw}$ is calculated from the raw (unprocessed) time series data for each time step, not to be confused with $\mathcal{S}_{MVAB}$. One of the most striking features is the disparity between the KH and non-KHI events for the magnetosheath data, as demonstrated in Figures 13c and 13f, respectively.

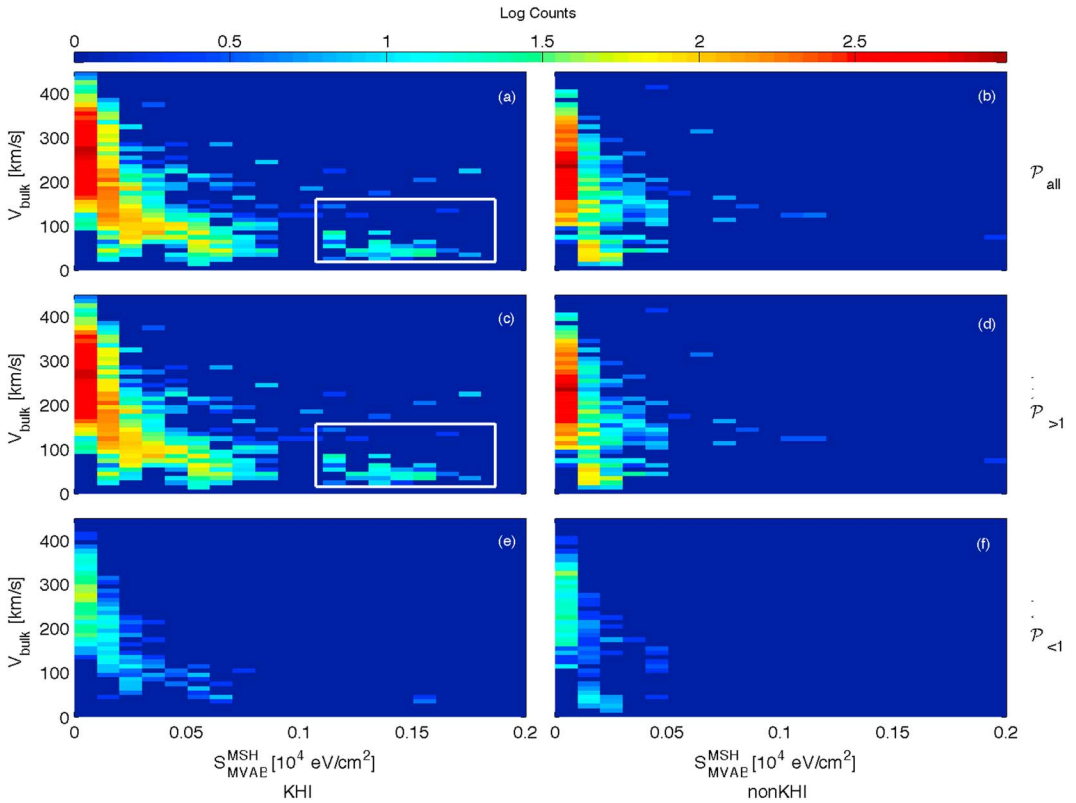

Figure 14. The 2-D distributions of bulk plasma velocity V_{bulk} versus MSH MVAB specific entropy $\mathcal{S}^{MSH}_{MVAB}$ for the (a, c, and e) KH and (b, d, and f) non-KH events. Data filtered by all $\mathcal{P}$ (Figures 14a and 14b), $\mathcal{P} > 1$ (Figures 14c and 14d), and $\mathcal{P} < 1$ (Figures 14e and 14f).

Table 2
Log-Mean Specific Entropy Ratios Relating the Raw and Ion-Scale Wave Intervals

	n	$\frac{\langle S^n_{MVAB}\rangle}{\langle S^{MSP}_{raw}\rangle}$	$\frac{\langle S^n_{MVAB}\rangle}{\langle S^{MIX}_{raw}\rangle}$	$\frac{\langle S^n_{MVAB}\rangle}{\langle S^{MSH}_{raw}\rangle}$
KHI	MSP	0.942	3.61	57.0
	MIX	0.211	**0.811**	12.8
	MSH	0.0171	0.0657	**1.04**
non-KHI	MSP	**0.414**	1.61	24.5
	MIX	0.290	**1.13**	17.2
	MSH	0.0530	0.122	**3.14**

Note. The bold values along the diagonals correspond to the ratio of the raw log-mean specific entropy in plasma of type n to its corresponding MVAB value.

There exists a population of low speed, high specific entropy plasma in the MSH during the KH events that is not present during the non-KH events. The low bulk velocity profile of this high specific entropy ion population suggests that it resides in close vicinity to the magnetopause. It is likely that this enhanced $\mathcal{S}^{MSH}_{raw}$ population is a result from one of the following: (i) reflection of KAWs back into the MSH as suggested by the KH event magnetic compressibility profile, (ii) plasma transport from the MSP to MSH due to magnetic reconnection associated with the KHI, or (iii) a combination of (i) and (ii). To address the hypothesis posed in (i), the (ion-scale) specific entropy $\mathcal{S}^{MSH}_{MVAB}$ is plotted as a function of bulk velocity and $\mathcal{P}$ in Figures 14a–14f. Following the $\mathcal{S}^{MSH}_{MVAB}$ distributions for all $\mathcal{P}$ and $\mathcal{P} > 1$, the enhanced $\mathcal{S}^{MSH}_{MVAB}$ population is still present as seen in Figures 14a and 14c. However, when considering $\mathcal{P} < 1$, this enhanced $\mathcal{S}^{MSH}_{MVAB}$ population vanishes as shown in Figure 14e. This is particularly significant because KAWs are confined by $\mathcal{P} \geq 1$—the fact that this enhanced $\mathcal{S}^{MSH}_{MVAB}$ population is not present when filtering out $\mathcal{P} > 1$ suggests that this low bulk velocity, high specific entropy population might be created at least in part by the reflection of mode converted KAWs back into the MSH. It should be noted that this enhanced $\mathcal{S}^{MSH}_{raw}$ ($\mathcal{S}^{MSH}_{MVAB}$) population from Figure 13c (Figure 14a) is heavily influenced by the 3 July 2001 event in which Nykyri et al. (2006) reported evidence of magnetic reconnection inside KH vortices and associated parallel ion beams. Furthermore, this enhanced $\mathcal{S}^{MSH}_{MVAB}$ population occurs in sufficiently low β ($\beta < 0.1$)—a requirement for significant specific entropy increase associated with magnetic reconnection (Ma & Otto, 2014). Therefore, it is reasonable to speculate that the this enhanced $\mathcal{S}^{MSH}_{raw}$ population is produced by plasma transport from reconnection inside the KH vortices and the reflection of KAWs.

The calculated log-mean specific entropies $\langle S^n_{raw}\rangle$ are listed in Table 1 for the MSP, MIX, and MSH plasma regions along with their ratios relative to the MSH $\langle S^n_{raw}\rangle/\langle S^{MSH}_{raw}\rangle$ and the percentage of data points greater than $\langle S^{MSH}_{raw}\rangle$ by at least a factor of 5 both for (P^n_{raw}) and the ion-scale wave intervals (P^n_{MVAB}). Another interesting feature is how the ratios of raw log-mean specific entropies are strikingly similar for the KH and non-KH events as shown in Table 1.

Comparisons between the raw and MVAB interval log-mean specific entropies are provided in Table 2. For each plasma region, the ratio of the log-mean specific entropies between the raw and ion-scale wave intervals ($\langle S^n_{MVAB}\rangle/\langle S^n_{raw}\rangle$), where n represents the plasma region, calculated during the KH events is much closer to unity when compared to the non-KH events (see diagonals from Table 2). For example, in the MSP plasma (n = MSP) $\langle S^{MSP}_{MVAB}\rangle/\langle S^{MSP}_{raw}\rangle$ is 0.942 and 0.414 for the KH and non-KH events, respectively. This means that the specific entropy calculated in the ion-scale wave intervals offers a more quantitatively accurate description of the raw specific entropy during the KH events compared to the non-KH events. In other words there is a better correlation between $\langle S^n_{MVAB}\rangle$ and $\langle S^n_{raw}\rangle$ when KH is active.

4. Discussion

In the present work, ion-scale properties for KH and non-KH events were compared. Cluster data from magnetopause crossings were binned according to their relative ion energies in order to compare ion-scale wave properties in the magnetosphere, magnetosheath, and mixed plasmas. These ion-scale properties are compared to previous observations of ion-scale wave activity from Moore et al. (2016), specifically a FMW interval associated with ion heating inside a rolled-up KH vortex. In Figures 3a–3d, the degree of polarization ϵ above and below f_{ic} was shown for the KH and non-KH events. The peaks in the $|\epsilon|$ PDFs, at approximately $\pm$0.675, are in good agreement with ion-scale wave activity from Moore et al. (2016), where ellipticities were calculated between approximately 0.57 and 0.66 for waves identified to be FMW and KAW. Without the ability to accurately assess the handedness of these waves in a statistical manner, the weight of right to left handedness in the degree of polarization between the KH and non-KH events remains indistinguishable.

The magnetic compressibility was presented in section 3.1.2; there is an amplification in the transverse wave power when transitioning from the MSH to MIX to MSP plasmas that is only present for the non-KH events as shown in Figure 4 (right). It is most likely that there is significant reflection of KAWs back into the MSH

associated with mode conversion (Johnson & Cheng, 1997; Johnson et al., 2001) during the KH events such that this amplification is not observed. Ion-scale waves identified using a sliding window MVAB were shown in section 3.2 with their respective properties. In Figures 6 (top to bottom) the comparison in the total magnetic wave power between the KH and non-KH events was presented for the MSP, MIX, and MSH plasmas, respectively. There is an apparent transition in the comparisons between the low power band of quasi-perpendicular waves from the MSH to the MIX and MSP plasmas where observations go from non-KH to KH dominant, respectively. In the MSH plasma the low power waves are non-KH dominant for all propagation angles. In the MIX and MSP plasmas the low power oblique waves are KH dominant, where the KH dominance extends to the high power waves in the MSP. Furthermore, there are relatively more KH dominant high power wave observations in the MSP plasma region. The lower power waves shown in the MIX and MSP plasma regime for the quasi-perpendicular waves are consistent with the observed quasi-perpendicular FMW observed inside the center of the KH vortex from Moore et al. (2016). The quasi-perpendicular ($\theta_{kB} = 85°, 88°$) FMWs observed on 6 June 2002 by Moore et al. (2016) in the center of a KH vortex have a magnetic wave amplitude range of approximately 0.3–0.6 nT/Hz$^{1/2}$ that corresponds to $|\delta B_{\text{tot}}|^2 \approx 0.09–0.36$ nT^2/Hz. Recall that the binning algorithm discussed earlier sets approximately 75% of the FMW interval into the MIX bin and the remaining 25% into the MSP bin.

The difference in total integrated Poynting flux between the KH and non-KH events for the MSP, MIX, and MSH plasmas was depicted in Figures 7 (top to bottom), respectively. There is a clear non-KH dominance in the available wave energy among the quasi-perpendicular waves in the MSH. However, a transition occurs in the MIX plasma, where the wave energy among the quasi-perpendicular waves becomes KH dominant for the lower band of S_{int}. This transition results in KH-dominant quasi-perpendicular waves for all S_{int} in the MSP plasma. This appears to be connected to the enhancement of KH-dominant quasi-perpendicular wave power in the MIX and MSP plasmas from the MSH discussed above. This transition in the total magnetic wave power and total integrated Poynting flux suggests that more quasi-perpendicular waves and their associated wave energy are more accessible to the MSP plasma when KHI is active. KAWs can heat ions stochastically (Johnson & Cheng, 2001) and have been shown to transfer significant energy into the magnetosphere (Chaston et al., 2007) when KHI is active. KH vortex associated FMWs have also been shown to heat cold component ions (Moore et al., 2016).

The KH-dominant observations of quasi-perpendicular waves in the MSP and MIX plasma, shown in Figure 9 (top and middle), respectively, might not appear to be consistent with the much higher value of S_{int} calculated from the FMW interval; however, when considering the MVAB window length compared to the actual FMW interval duration, the results are in good agreement. The FMW interval is approximately 18.4 s in duration with a local average $f_{\text{ic}} \approx 0.3$ Hz (Moore et al., 2016). Because the MVAB window length is dependent upon f_{ic} and search is limited to $[f_{(j_{\text{ic}}-10)}, f_{(j_{\text{ic}}+10)}]$, the window range over the FMW interval is bound by an approximate 0.20–0.45 Hz restriction. This restricts the possible MVAB window lengths passing over the FMW interval to approximately 2.2–5 s, which corresponds to a maximum of 27% of the actual FMW interval length. A crude estimation assumes that only 27% of the actual FMW S_{int} is recorded in the 2-D distribution plot of the S_{int} versus propagation angle, which is approximately only 1.2×10^6 keVcm^{-2}. This scaled estimate makes the KHI dominant wave observations in the MSP plasma regime consistent with the FMW observations from Moore et al. (2016).

In Figure 8, the scaled wave electric to wave magnetic field ratio was presented for the FMW wave interval, which includes data from the MSP and MIX plasmas. The distribution is shown to be quite broad (approximately $0 \leq (|\delta E_\perp|/|\delta B_\perp|)/v_A \leq 8$) near the local ion cyclotron frequency ($f_{\text{ic}} \approx 0.3$ Hz). Additionally, the comparison of $\mathcal{P}$ between the KH and non-KH events was provided for the MSP, MIX, and MSH plasmas in Figures 9 (top to bottom). In the MSH plasma, the KH-dominant distribution consists of a narrowband ($\mathcal{P} \leq 3$) for all propagation angles. This KH-dominant distribution widens in $\mathcal{P}$ space for the quasi-perpendicular wave observations in the MIX and MSP plasma regimes. The quasi-perpendicular $\mathcal{P}$ observations from the MSP and MIX plasma regimes were shown to be consistent with FMW observations from Moore et al. (2016). Additionally, the $\mathcal{P}$ observations are consistent with KAWs for both the KH and non-KH-dominant wave observations; KAW observations have been shown to have a wave electric to wave magnetic field ratio grater than or equal to the Alfvén velocity for sub-ion cyclotron frequencies (Chaston et al., 2007, 2012). Similar to the wave power and Poynting flux distributions, there is a transition from the KH-dominant trend in the MSH beginning in the MIX plasma, where the $\mathcal{P}$ distribution begins to widen (especially for the quasi-perpendicular component) in the MIX plasma and broadens even further in the MSP plasma. The broad KH-dominant

distributions in $\mathcal{P}$ at oblique angles ($\theta_{kB} = 40° - 90°$) for the MSP and MIX plasma regimes are consistent with the FMW $\mathcal{P}$ distribution in the vicinity of the local ion cyclotron frequency. The portion of the KH-dominant $\mathcal{P}$ distributions among the quasi-perpendicular waves in the MIX and MSP plasmas is consistent with both the FMW interval and KAWs.

Presented in Figures 10 (left and right) and 11 (left and right) were the plasma beta profiles for the ion-scale wave intervals and raw plasma beta profiles for the MSH plasma β_{raw}^{MSH}, respectively. It was shown that although the β_{raw}^{MSH} is statistically lower during the KH events, it is not sufficiently low (required $\beta << 1$), so that reconnection and associated shocks could account for the level of observed nonadiabtic heating (Ma & Otto, 2014). Furthermore, the high raw beta in the MSH during the non-KH events might explain why KHI is inactive. Compressibility and magnetic tension are known to stabilize KHI (Miura & Pritchett, 1982); compressibility can result from high plasma pressure and velocity in the magnetosheath.

In the later portion of section 3.2.5, the specific entropy results from the raw and ion-scale wave intervals were shown and discussed. It was shown from Figure 12 that there is significant increase in the specific entropy related to the ion-scale wave intervals during the KH events. One conclusion that is drawn from this result is as follows: there is more nonadiabatic heating across the magnetopause associated with ion-scale wave activity when KHI is active at the boundary compared to when it is inactive. It was also shown that the KH active MSH hosts an enhance specific entropy population, and that this "preheated" plasma is most likely generated from a combination of KAW reflection and magnetic reconnection inside the KH vortices. Although non-KH event P_{raw}^{MSP} profile from Table 1 shows a similar increase in specific entropy from the MSH to the MSP plasma as the KH events, it should be noted that the specific entropy calculation does not differentiate between the cold and hot component ions. In fact, southward IMF can contribute to the formation of a hot and tenuous plasma sheet (Wing & Newell, 2002). Plasma energization in the plasma sheet related to substorm activity is well known (Hones Jr. et al., 1976)—ion (Hietala et al., 2015; Runov et al., 2009) and electron (Runov et al., 2009) heating has been shown in plasma flow channels in the magnetotail. Furthermore, a hot and tenuous plasma sheet would have a higher specific entropy than a cold and dense plasma sheet. From Table A1, the time-lagged OMNI data show that several of the non-KH events possess a significant southward component in the IMF of the upstream solar wind that may drive reconnection in the magnetotail and generate bursty bulk flows.

There is significant evidence of strong nonadiabatic heating directly related to ion-scale wave activity when KHI is active. Additionally, the heightened wave energy from the obliquely propagating ion-scale waves suggests that more energy is available to the MSP when KHI is active. These results suggest that ion-scale waves, such as observed and studied in detail by Moore et al. (2016), could strongly contribute to this significant nonadiabatic heating observed across the magnetopause during KHI events. Moore et al. (2016) observed the specific entropy increase by a factor of approximately 3 over the short FMW interval observed inside of a KH vortex and aproximately 1.4 orders of magnitude relative to the magnetosheath during the entire 2 min duration of the ion-scale wave activity. The temperature of the cold-component ion population during this brief wave period increased by 2 keV.

5. Conclusions

This present work identified ion-scale wave properties associated with magnetopause crossings in the low-latitude flanks during periods where KHI was active and inactive and addressed the ubiquity of nonadiabatic heating to KHI. The conclusions can be summarized as follows:

1. The obliquely propagating waves have more power in the MSP-like plasma regions when KHI is present.
2. Increase in the specific entropy associated with ion-scale waves is more pronounced when KHI is present.
3. Although the raw MSH plasma beta is lower ($\beta_{raw}^{MSH} < 1$) during the KH events, it is not sufficiently low enough to account for nonadiabatic heating from reconnection and associated shocks.
4. The KH and non-KH-dominant observations of the scaled wave electric to magnetic field ratio distributions are consistent with KAWs in the MSP, MIX, and MSH plasmas.

This seems to indicate that, under KHI, more (ion-scale) wave energy is available to the MSP that could be responsible for wave heating. Furthermore, comparison of the statistical wave properties with the FMW interval and ion-scale wave intervals in Moore et al. (2016) shows the following:

1. The mean total magnetic wave power observed during the FMW interval in Moore et al. (2016) falls within the range of KH-dominant observations of quasi-perpendicular propagating waves in the MIX and MSP plasma.
2. In the MSP plasma, the estimated total integrated Poynting flux calculated during the FMW interval in Moore et al. (2016) falls within the range of KH-dominant observations of quasi-perpendicular propagating waves.
3. The broad distributions in the $\delta E/\delta B$ ratio scaled by the local Alfvén velocity for the KH-dominant quasi-perpendicular ion-scale wave activity are consistent with the FMW interval in Moore et al. (2016).
4. Peaks in the degree of polarization during KH and non-KH events are consistent with the ion-scale waves observed by Moore et al. (2016).

In summary, there is a clear association between nonadiabatic heating and ion-scale wave activity when KHI is active. Among the ion-scale wave activity, a distinct KH dominance is shown for quasi-perpendicular waves whose properties are consistent with recently observed FMW activity and KAWs. Although the raw specific entropy is shown to increase from the MSH to MSP when KHI is inactive, the plasma sheet may already be populated by hot and tenuous plasma due to substorm activity. Solar wind effects on the source MSH plasma are unlikely a significant cause of the specific entropy increase associated with the ion-scale waves in the MSP plasma when KHI is active. Furthermore, taking into account Doppler shift effects has an insignificant effect on the total magnetic wave power, total integrated Poynting flux, and the scaled wave electric to wave magnetic field ratio. These findings may shed significant light on the origins of the plasma sheet temperature asymmetry of cold-component ions and nonadiabatic heating across the magnetopause. Energy provided in the form of a velocity shear can drive fluid-scale KH waves at the magnetopause. Previously, it has been shown that there is a sufficient energy surplus—leftover from the twisting of magnetic field and plasma compression from the KH motion—comparable to ion-scale FMW emissions capable of energizing ions via harmonic cyclotron resonance. These results suggest that waves, consistent with KH vortex associated FMW activity and KAWs, may play a significant role in the cross-scale energy transport between fluid and ion scales. However, more work is needed to uncover the mechanism by which these waves are generated inside the pressure wells of the KH vortices.

Appendix A: Effects of Solar Wind Speed on Plasma Parameters

It has been shown that certain plasma parameters in the magnetosheath can be effected by solar wind flows. Wang et al. (2012) revealed a correlation between magnetosheath ion temperatures (T_i) and ion to electron temperature ratios from a statistical study using 4 years of THEMIS data. They showed that higher solar wind speeds ($|V| > 450$ km/s) correspond to higher ion temperatures in the magnetosheath whereas lower solar wind speeds ($|V| < 450$ km/s) correspond to lower ion temperatures. In this section we explore the plausibility of contamination in the plasma parameters due to initial solar wind conditions by exploring how solar fast and slow wind speeds affect the seed population in the magnetosheath.

Average solar wind conditions are calculated from time-lagged OMNI data by averaging over timescales comparable to each event and are listed in Table A1. The "fast" solar wind speeds are highlighted in bold. In the context of this section fast and slow solar wind speeds are defined as $|V| > 400$ km/s and $|V| < 400$ km/s, respectively. Although the magnetic wave power in the solar wind is an important factor to consider, the temporal resolution is insufficient to accurately compare to the statistics performed within the ion cyclotron frequency range and thus has been omitted from Table A1. It is well known that the foreshock can act as a source for waves that convect into the magnetosheath (Blanco-Cano et al., 2006; Gutynska et al., 2015); however, inferring this information via tracing streamlines from point measurements to a reconstructed shock geometry (source region) (Génot et al., 2011) adds too much uncertainty and subsequent error to reliably be considered in this work.

Statistical mapping of the magnetosheath specific entropy in the magnetosheath interplanetary medium is performed using 5 years of THEMIS and OMNI data (Dimmock & Nykyri, 2013, Dimmock et al., 2014, 2015; Dimmock, Pulkkinen, et al., 2016). The specific entropy dependance on the solar wind speed can be seen in Figure A1, where the overall mean specific entropy in the magnetosheath is higher during fast (b) solar wind speeds compare to slow (a) solar wind speeds. There are noticeable enhancements in the mean specific entropy adjacent to the magnetopause (inner boundary) for both the solar wind speeds. However, comparing Figures A1a and A1b, this enhancement appears slightly wider for the fast solar wind, especially for the tailward populations.

AGU Journal of Geophysical Research: Space Physics

10.1002/2017JA024591

Table A1
Average Time-Lagged Solar Wind Data From OMNI

	Date (yyyy-mm-dd)	$\vec{B}$ (nT)	$\vec{V}$ (km/s)	n (cm^{-3})	T (10^6 K)	$\lvert B\rvert$ (nT)	$\lvert V\rvert$ (km/s)	β	M_A
KHI	2001-07-03	<3.88, −5.40, −0.52>	< −402.27, −15.62, −11.24>	8.11	0.09	8.49	**403.03**	1.03	6.77
	2001-11-20	< −3.06, 0.58, 2.75>	< −388.68, −41.87, −21.30>	3.82	0.10	4.20	391.50	2.07	9.15
	2002-06-06	<0.96, −4.95, −0.16>	< −367.12, −13.46, −11.08>	4.13	0.02	5.16	367.57	0.975	7.24
	2002-06-13	<2.79, −3.39, −4.62>	< −368.44, −0.34, −26.72>	5.81	0.05	6.78	369.57	0.929	6.58
	2004-06-19[a]	< −0.52, 3.73, 1.08>	< −472.56, 8.29, 8.27>	3.05	0.12	4.52	**472.99**	1.57	9.15
	2004-06-21	<0.96, 2.30, 1.21>	< −408.91, −2.82, 5.93>	3.67	0.06	3.70	**409.13**	2.11	10.6
non-KHI	2004-11-16	<2.02, −4.90, 1.95>	< −428.69, 19.00, 16.11>	7.26	0.16	7.37	**430.00**	1.67	7.94
	2004-11-27	< −2.36, 2.68, −4.05>	< −421.57, −21.99, −4.67>	5.40	0.08	6.43	**422.62**	1.11	7.64
	2005-06-28	< −2.18, 2.32, 0.10>	< −375.06, −5.55, 20.80>	9.41	0.05	3.38	375.70	6.60	17.6
	2007-06-04	<3.42, 1.84, 1.77>	< −478.45, 36.66, −2.14>	4.73	0.13	4.73	**479.94**	2.34	11.1
	2007-06-06	< −1.97, −0.31, −1.45>	< −347.99, 1.88, −7.79>	3.96	0.03	2.50	348.12	4.28	13.9
	2007-06-06	< −2.03, 1.20, -0.80>	< −337.68, −1.77, −3.58>	4.14	0.03	2.67	337.76	3.93	12.9
	2009-06-03	<0.79, 0.45, 1.51>	< −303.62, −0.69, −4.02>	7.67	0.02	2.28	303.67	11.2	19.5
	2009-06-26	<3.29, 0.80, −0.49>	< −449.43, 25.56, −2.55>	2.92	0.10	3.50	**450.19**	2.32	11.0

[a]This event was considered PS by Moore (2012) due to differing techniques in averaging solar wind data.

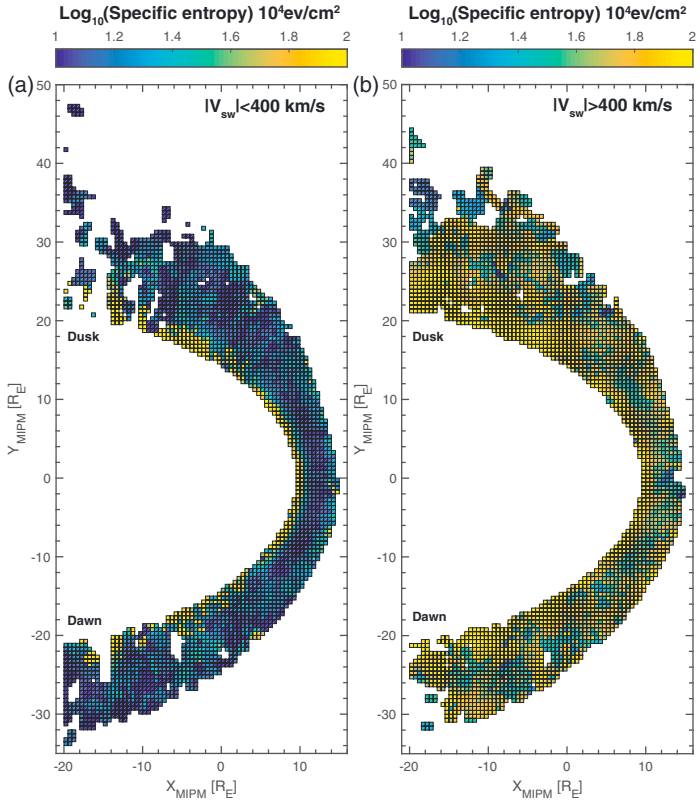

Figure A1. Mean of the mean specific entropy maps for (a) slow and (b) fast solar wind using THEMIS data.

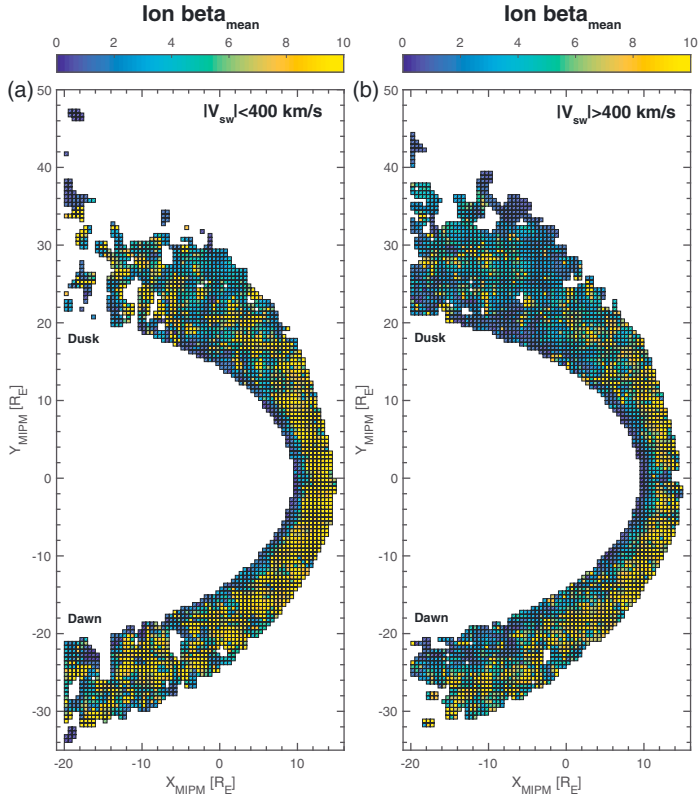

Figure A2. Mean of the mean plasma beta maps for (a) slow and (b) fast solar wind using THEMIS data.

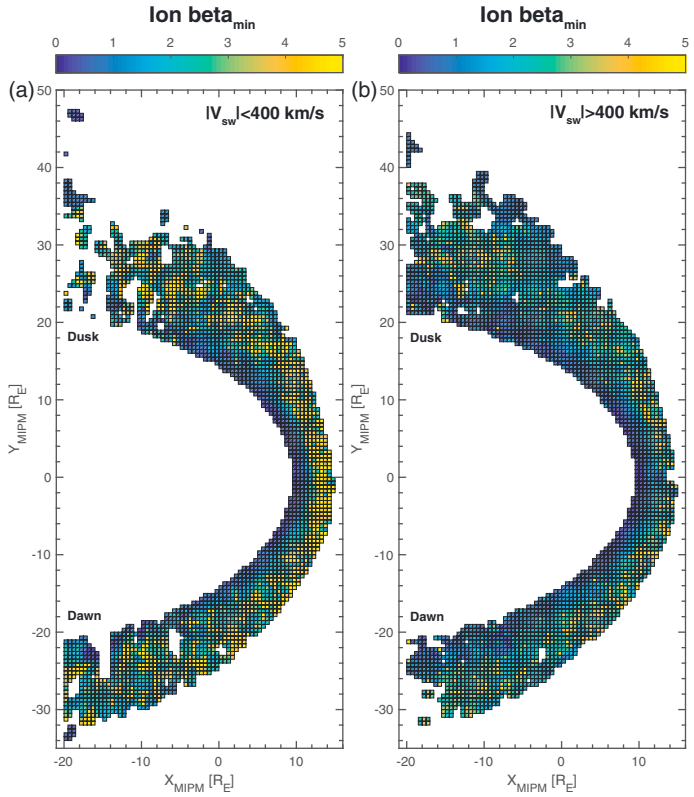

Figure A3. Mean of the minimum plasma beta maps for (a) slow and (b) fast solar wind using THEMIS data.

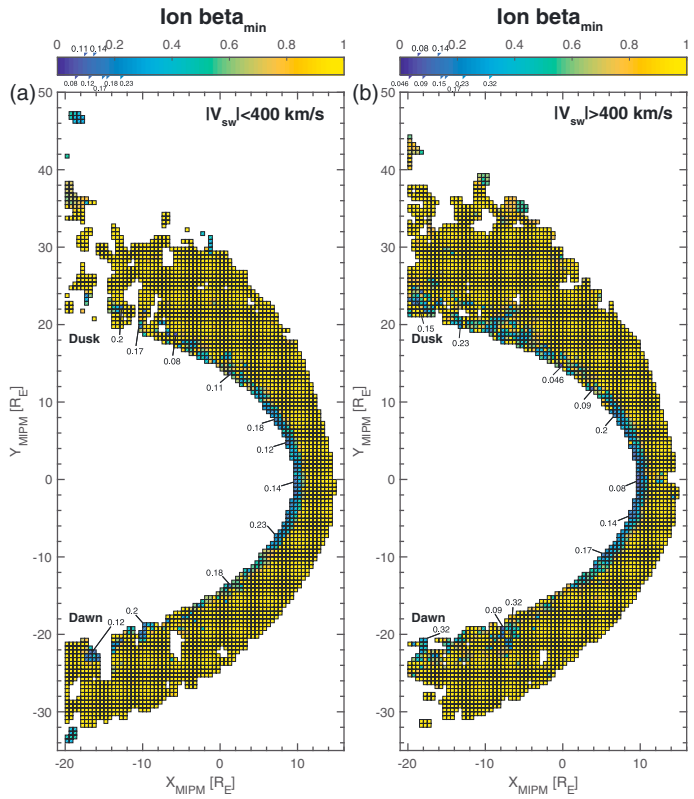

Figure A4. Saturated scale of the mean of the minimum plasma beta maps for (a) slow and (b) fast solar wind using THEMIS data.

Although the magnitude of the solar wind velocity seems to be correlated to the specific entropy in the magnetosheath plasma, it is unlikely that these effects contribute to the relative specific entropy increases observed in either the raw or MVAB wave intervals discussed in section 3.2.5. This is mostly because the $< \mathcal{S}_{\text{raw}}^{\text{MSH,KHI}} >$ is in fact higher than $< \mathcal{S}_{\text{raw}}^{\text{MSH,nonKHI}} >$ even though the average solar wind speed for all of the KH events is lower than that of the non-KH events.

Plasma beta dependence on the solar wind speed is depicted in Figures A2a and A2b and A3a and A3b for the mean and minimum plasma beta, respectively, where at first glance the plasma beta is larger for slower wind speeds in the central magnetosheath and near the bow shock. For both solar wind speeds, the lowest mean and minimum plasma beta populations are located in the vicinity of the magnetopause corresponding to the enhancements in the mean specific entropy from Figures A1a and A1b.

There appears to be little solar wind speed dependence on the mean plasma beta when comparing the region adjacent to the magnetopause in Figures A2a and A2b except for a slightly wider low minimum beta population for the fast solar wind, especially farther tailward; this is more evident when comparing Figures A3a and A3b. Saturating the color bar from Figures A3a and A3b gives a more detailed description of the minimum plasma beta range along the magnetopause depicted in Figures A4a and A4b. In Figures A3a and A3b, there are more populations of very low plasma beta ($\beta < 0.1$) when the solar wind is fast (Figure A3b) compared to when it is slow (Figure A3a).

These data suggest that there is a correlation between the specific entropy enhancements in the magnetosheath along the magnetopause and the plasma beta, with subtle variation when considering solar wind speed. The plasma beta adjacent to the magnetopause is slightly lower for faster solar wind and corresponds to larger enhancements in the specific entropy along the magnetosheath side of the magnetopause. On average, the plasma beta along the magnetopause is not sufficiently low ($\beta < 0.1$) to account for a significant increase in the specific entropy in the magnetosphere from magnetic reconnection (Ma & Otto, 2014). However, there exists a larger population that might satisfy the low plasma beta requirement when the solar wind is fast—Ma and Otto (2014) showed that $\beta = 0.025$ in the inflow region (magnetosheath) was sufficiently low to increase the specific entropy in the outflow region (magnetosphere) by a factor of 4. It is most likely that the raw specific increase for the non-KH events is produced in part by magnetic reconnection and substorm activity.

Appendix B: Doppler Shift Effects

In an aim to estimate possible Doppler effects, the wave vector **k** is assumed to take on two possible forms governed by the FMW and KAW dispersion relations defined in equations (B1) and (B2), respectively. $\mathbf{k}_{\text{FMW}}$ is determined for each ion-scale (MVAB) wave interval by solving equation (B1) when $\omega = \omega_{\text{ic}}$. Similarly, $\mathbf{k}_{\text{KAW}}$ is determined for each ion-scale (MVAB) wave interval by solving equation (B2) when $\omega = 0.9\omega_{\text{ic}}$—a factor of 0.9 is used because the KAW dispersion relation is asymptotic at ω_{ic}. The resulting Doppler shift is then calculated for the FMW and KAW cases using the Doppler shift equation $\omega_p = \omega_{\text{sc}} - \mathbf{k} \cdot \vec{v}_{\text{bulk}}$, where ω_p is the plasma frame angular frequency, ω_{sc} is the spacecraft frame angular frequency, and $\vec{v}_{\text{bulk}}$ is the bulk plasma velocity in the spacecraft frame.

$$\omega^2 = \frac{k^2}{2}\left(c_{\text{ms}}^2 + \left[\left(v_A^2 - c_s^2\right)^2 + 4v_A^2 c_s^2 \frac{k_\perp^2}{k^2}\right]^{1/2}\right) \tag{B1}$$

$$\omega = k_{||} v_A \omega_{\text{ic}} \sqrt{\frac{1 + k_\perp^2\left(\rho_s^2 + \rho_i^2\right)}{\omega_{ic}^2 + k_{||}^2 v_A^2\left(1 + k_\perp^2 \rho_i^2\right)}} \tag{B2}$$

Figures B1–B3 show how the possible Doppler shifts may effect the 2-D mean magnetic wave power, total integrated Poynting flux, and mean scaled $\delta E/\delta B$ comparative distributions with the k_{FMW} assumption. Figures B1–B3 (left, middle, and right columns) correspond to a parallel Doppler shift, no Doppler shift, and antiparallel Doppler shift, respectively. Similarly Figures B4–B6 show possible Doppler shift effects on the 2-D distributions with the k_{KAW} assumption.

Taking into account the parallel Doppler shift has an insignificant effect on the properties of the 2-D mean magnetic wave power, total integrated Poynting flux, and mean scaled $\delta E/\delta B$ comparative distributions

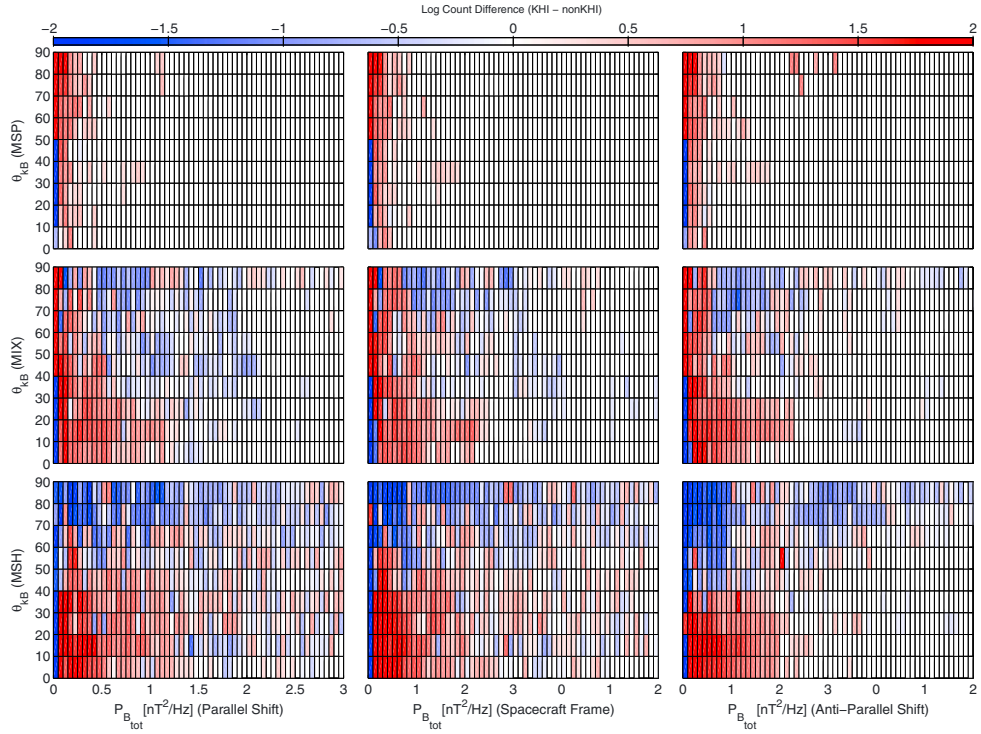

Figure B1. FMW estimated (left column) parallel $\hat{k}$ and (right column) antiparallel $\hat{k}$ Doppler effects on the 2-D comparative distributions of mean total power (P_{tot}) versus propagation angle (θ_{kB}) between KHI and non-KHI events. (middle column) The non-Doppler shifted distributions. Figure B1 (top to bottom rows) represents the MSP, MIX, and MSH plasma regimes, respectively.

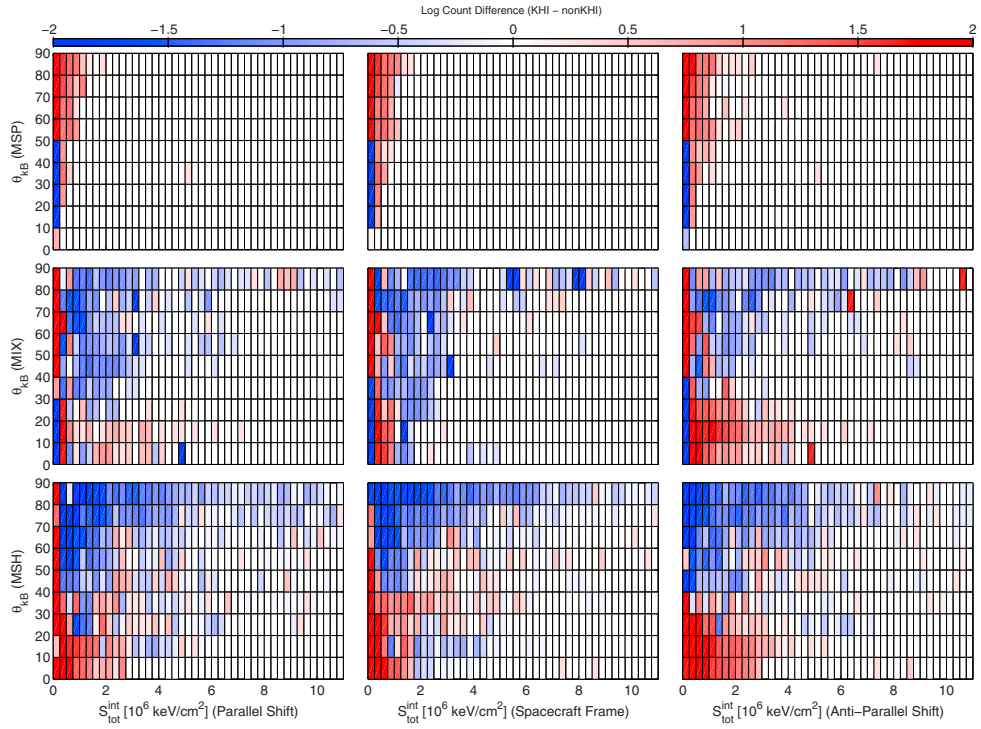

Figure B2. FMW estimated (left column) parallel $\hat{k}$ and (right column) antiparallel $\hat{k}$ Doppler effects on the 2-D comparative distribution of the integrated Poynting flux versus propagation angle (S_{int} versus θ_{kB}). (middle column) The non-Doppler shifted distributions. Figure B2 (top to bottom rows) represents MSP, MIX, and MSH plasma regimes, respectively.

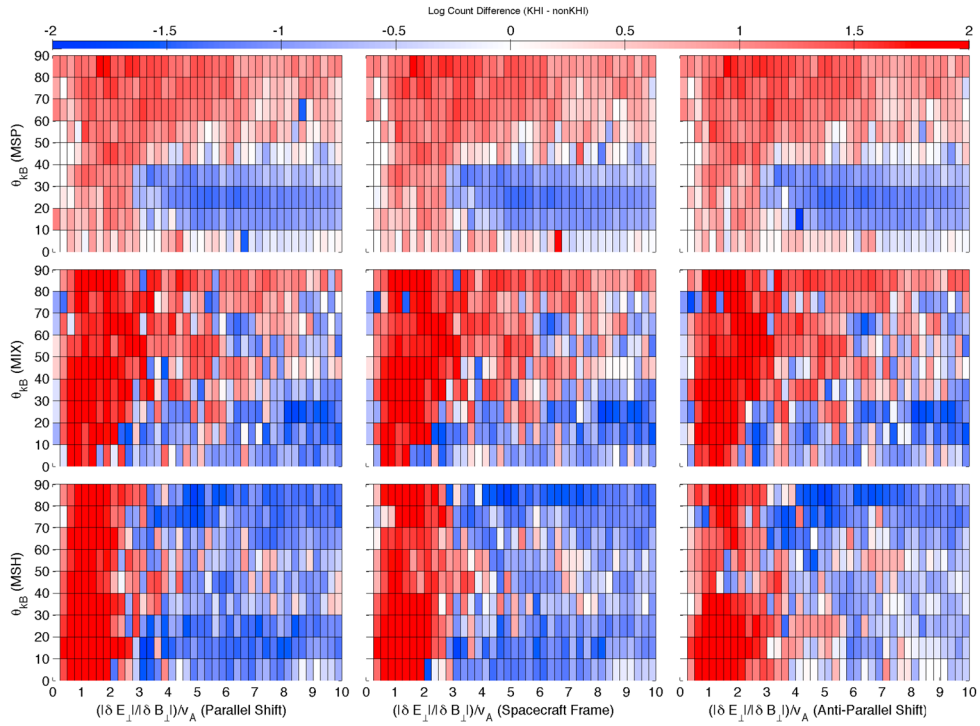

Figure B3. FMW estimated (left column) parallel $\hat{k}$ and (right column) antiparallel $\hat{k}$ Doppler effects on the 2-D comparative distributions of scaled mean wave electric to magnetic field ratio versus propagation angle. (middle column) The non-Doppler shifted distributions. Figure B3 (top to bottom rows) represents the MSP, MIX, and MSH plasma regimes, respectively.

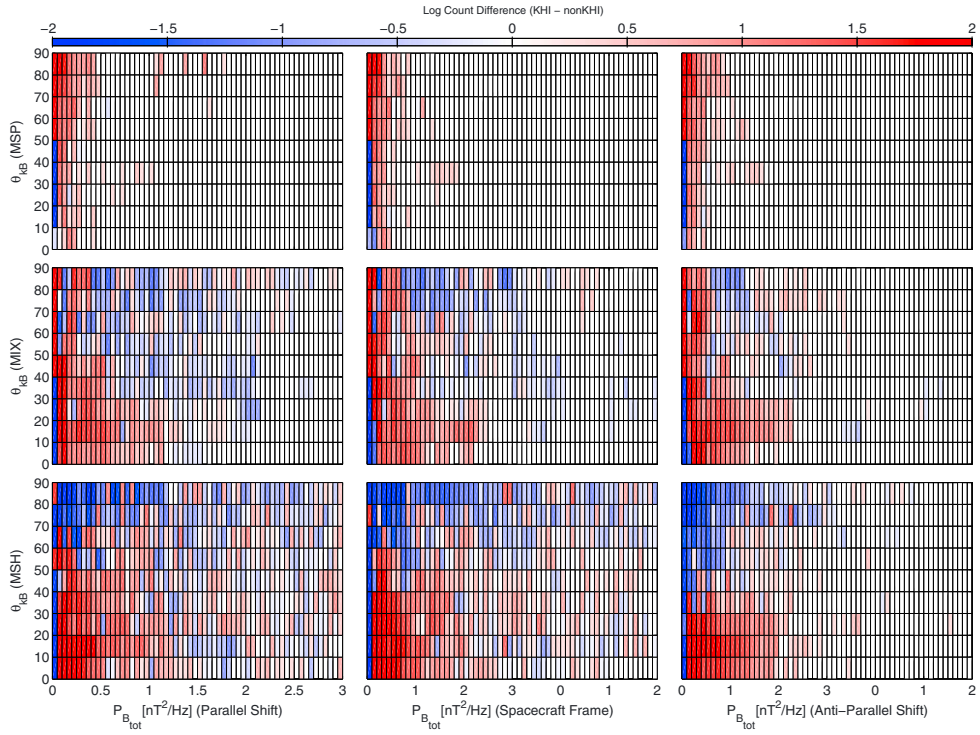

Figure B4. KAW Estimated (left column) parallel $\hat{k}$ and (right column) antiparallel $\hat{k}$ Doppler effects on the 2-D comparative distributions of mean total power (P_{tot}) versus propagation angle (θ_{kB}) between KHI and non-KHI events. (middle column) The non-Doppler shifted distributions. Figure B4 (top to bottom rows) represents the MSP, MIX, and MSH plasma regimes, respectively.

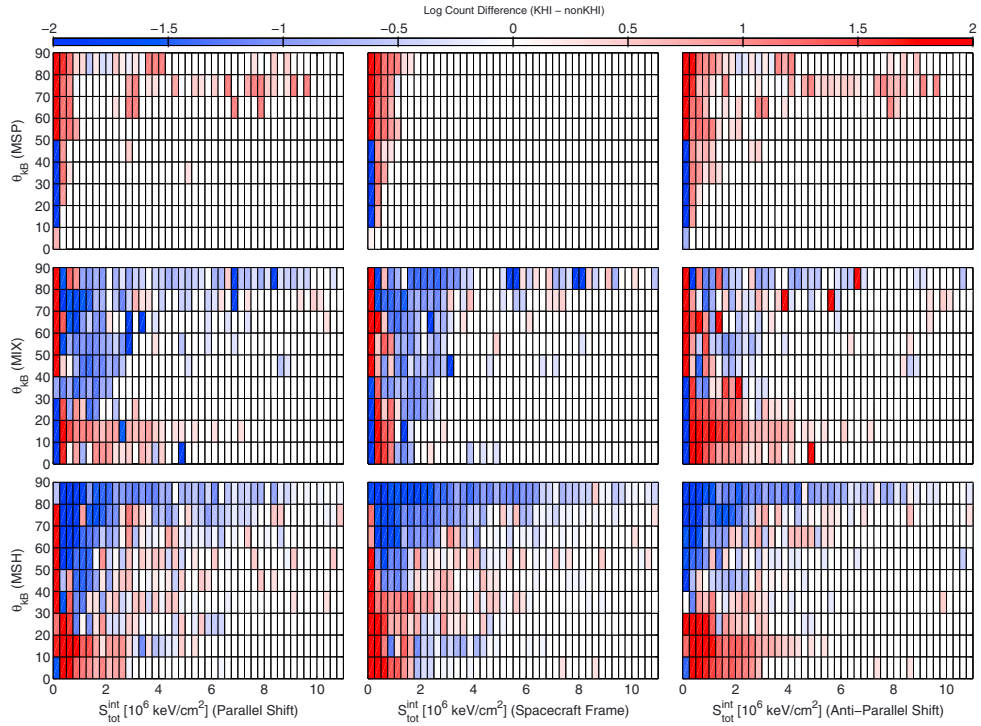

Figure B5. KAW estimated (left column) parallel $\hat{k}$ and (right column) antiparallel $\hat{k}$ Doppler effects on the 2-D comparative distribution of the integrated Poynting flux versus propagation angle (S_{int} versus θ_{kB}). (middle column) The non-Doppler shifted distributions. Figure B5 (top to bottom rows) represents the MSP, MIX, and MSH plasma regimes, respectively.

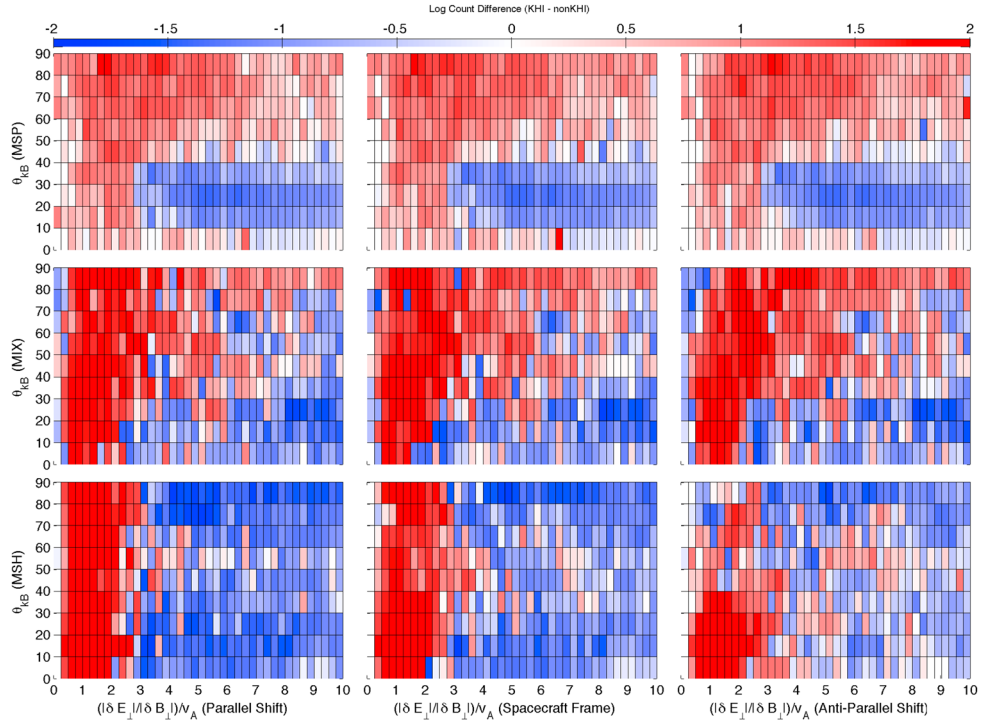

Figure B6. KAW estimated (left column) parallel $\hat{k}$ and (right column) antiparallel $\hat{k}$ Doppler effects on the 2-D comparative distributions of scaled mean wave electric to magnetic field ratio versus propagation angle. (middle column) The non-Doppler shifted distributions. Figure B6 (top to bottom rows) represents the MSP, MIX, and MSH plasma regimes, respectively.

(see Figures B1–B3 and Figures B4–B6, left columns). Similarly, the estimated antiparallel Doppler shift has an insignificant effect on the properties of the 2-D mean magnetic wave power, total integrated Poynting flux, and mean scaled $\delta E/\delta B$ comparative distributions (see Figures B1–B3 and Figures B4–B6, right columns).

Acknowledgments
Work by T. M. and K. N. was supported by the National Science Foundation (NSF) grant [10.13039/100000001] (1502774), and part of work by K. N. was supported by the National Aeronautics and Space Administration (NASA) grant [10.13039/100000104] (NNX16AF89G). Work by A. D. was supported by the Academy of Finland grant: Suomen Akatemia|Luonnontieteiden ja Tekniikan Tutkimuksen Toimikunta (Forskningsrådet för Naturvetenskap och Teknik) [10.13039/501100005877] (288472). The authors would like to acknowledge the work performed by the Cluster FGM, EFW, CIS, and PEACE instrument teams as well as the Cluster Science Archive and the Cluster Active Archive for the use of their data. Cluster data (Laakso et al., 2010) are available on the European Space Agency (ESA) website (http://www.cosmos.esa.int/web/csa). All other data are available from the authors upon request.

References

Balogh, A., Dunlop, M. W., Cowley, S. W. H., Southwood, D. J., Thomlinson, J. G., Glassmeier, K. H., … Kivelson, M. G. (1997). The Cluster magnetic field investigation. *Space Science Reviews*, *79*, 65–91.

Blanco-Cano, X., Omidi, N., & Russell, C. T. (2006). Macrostructure of collisionless bow shocks: 2. ULF waves in the foreshock and magnetosheath. *Journal of Geophysical Research*, *111*, A10205. https://doi.org/10.1029/2005JA011421

Borovsky, J. E., & Cayton, T. E. (2011). Entropy mapping of the outer electron radiation belt between the magnetotail and geosynchronous orbit. *Journal of Geophysical Research*, *116*, A06216. https://doi.org/10.1029/2011JA016470

Carozzi, T. D., Thidé, B., Leyser, T. B., Komrakov, G., Frolov, V., Grach, S., & Sergeev, E. (2001). Full polarimetry measurements of stimulated electromagnetic emissions: First results. *Journal of Geophysical Research*, *106*(A10), 21,395–21,407. https://doi.org/0.1029/2001JA900004

Chaston, C. C., Wilber, M., Mozer, F. S., Fujimoto, M., Goldstein, M. L., Acuna, M., … Fazakerley, A. (2007). Mode conversion and anomalous transport in Kelvin-Helmholtz vortices and kinetic Alfvén waves at the Earth's magnetopause. *Physical Review Letters*, *99*(17), 175004. https://doi.org/10.1103/PhysRevLett.99.175004

Chaston, C. C., Johnson, J. R., Wilber, M., Acuna, M., Goldstein, M. L., & Reme, H. (2009). Kinetic Alfvén wave turbulence and transport through a reconnection diffusion region. *Physical Review Letters*, *102*, 015001. https://doi.org/10.1103/PhysRevLett.102.015001

Chaston, C. C., Bonnell, J. W., Clausen, L., & Angelopoulos, V. (2012). Energy transport by kinetic-scale electromagnetic waves in fast plasma sheet flows. *Journal of Geophysical Research*, *117*, A09202. https://doi.org/10.1029/2012JA017863

Dimmock, A. P., & Nykyri, K. (2013). The statistical mapping of magnetosheath plasma properties based on THEMIS measurements in the magnetosheath interplanetary medium reference frame. *Journal of Geophysical Research: Space Physics*, *118*, 4963–4976. https://doi.org/10.1002/jgra.50465

Dimmock, A. P., Osmane, A., Pulkkinen, T. I., Nykyri, K., & Kilpua, E. (2017). Temperature variations in the dayside magnetosheath and their dependence on ion-scale magnetic structures: THEMIS statistics and measurements by MMS. *Journal of Geophysical Research: Space Physics*, *122*, 6165–6184. https://doi.org/10.1002/2016JA023729

Dimmock, A. P., Nykyri, K., & Pulkkinen, T. I. (2014). A statistical study of magnetic field fluctuations in the dayside magnetosheath and their dependence on upstream solar wind conditions. *Journal of Geophysical Research: Space Physics*, *119*, 6231–6248. https://doi.org/10.1002/2014JA020009

Dimmock, A. P., Nykyri, K., Karimabadi, H., Osmane, A., & Pulkkinen, T. I. (2015). A statistical study into the spatial distribution and dawn-dusk asymmetry of dayside magnetosheath ion temperatures as a function of upstream solar wind conditions. *Journal of Geophysical Research: Space Physics*, *120*, 2767–2782. https://doi.org/10.1002/2014JA020734

Dimmock, A. P., Pulkkinen, T. I., Osmane, A., & Nykyri, K. (2016). The dawn-dusk asymmetry of ion density in the dayside magnetosheath and its annual variability measured by THEMIS. *Annales Geophysicae*, *34*, 511–528. https://doi.org/10.5194/angeo-34-511-2016

Dimmock, A. P., Nykyri, K., Osmane, A., & Pulkkinen, T. I. (2016). Statistical mapping of ULF Pc3 velocity fluctuations in the Earth's dayside magnetosheath as a function of solar wind conditions. *Advances in Space Research*, *58*, 196–207. https://doi.org/10.1016/j.asr.2015.09.039

Eriksson, S., Lavraud, B., Wilder, F. D., Stawarz, J. E., Giles, B. L., Burch, J. L., … Goodrich, K. A. (2016). Magnetospheric multiscale observations of magnetic reconnection associated with Kelvin-Helmholtz waves. *Geophysical Research Letters*, *43*, 5606–5615. https://doi.org/10.1002/2016GL068783

Eriksson, S., Wilder, F. D., Ergun, R. E., Schwartz, S. J., Cassak, P. A., Burch, J. L., … Marklund, G. T. (2016). Magnetospheric multiscale observations of the electron diffusion region of large guide field magnetic reconnection. *Physical Review Letters*, *117*, 15001. https://doi.org/10.1103/PhysRevLett.117.015001

Escoubet, C. P., Schmidt, R., & Goldstein, M. L. (1997). Cluster—Science and mission overview. *Space Science Reviews*, *79*, 11–32. https://doi.org/10.1023/A:1004923124586

Fairfield, D. H., Otto, A., Mukai, T., Kokubun, S., Lepping, R. P., Steinberg, J. T., … Yamamoto, T. (2000). Geotail observations of the Kelvin-Helmholtz instability at the equatorial magnetotail boundary for parallel northward fields. *Journal of Geophysical Research*, *105*, 21,159–21,174. https://doi.org/10.1029/1999JA000316

Génot, V., Broussillou, L., Budnik, E., Hellinger, P., Trávníček, P. M., Lucek, E., & Dandouras, I. (2011). Timing mirror structures observed by Cluster with a magnetosheath flow model. *Annales Geophysicae*, *29*, 1849–1860. https://doi.org/10.5194/angeo-29-1849-2011

Gershman, D. J., Dorelli, J. C., DiBraccio, G. A., Raines, J. M., Slavin, J. A., oh, G., & Zurbuchen, T. H. (2016). Magnetic reconnection, Cusp, Field-aligned currents and current systems, Energetic particles: Precipitating, Mercury, reconnection, kinetic plasma, Mercury, polar cap, flux transfer event, flux rope. *Geophysical Research Letters*, *43*, 5935–5942. https://doi.org/10.1002/2016GL069163

Gustafsson, G., Bostrom, R., Holback, B., Holmgren, G., Lundgren, A., Stasiewicz, K., … Wygant, J. (1997). The electric field and wave experiment for the Cluster mission. *Space Science Reviews*, *79*, 137–156. https://doi.org/10.1023/A:1004975108657

Gutynska, O., Sibeck, D. G., & Omidi, N. (2015). Magnetosheath plasma structures and their relation to foreshock processes. *Journal of Geophysical Research: Space Physics*, *120*, 7687–7697. https://doi.org/10.1002/2014JA020880

Hasegawa, A., & Mima, K. (1978). Anomalous transport produced by kinetic Alfven wave turbulence. *Journal of Geophysical Research*, *83*, 1117–1123. https://doi.org/10.1029/JA083iA03p01117

Hasegawa, H., Fujimoto, M., Maezawa, K., Saito, Y., & Mukai, T. (2003). Geotail observations of the dayside outer boundary region: Interplanetary magnetic field control and dawn-dusk asymmetry. *Journal of Geophysical Research*, *108*(A4), 1163. https://doi.org/10.1029/2002JA009667

Hasegawa, H., Fujimoto, M., Phan, T.-D., Rème, H., Balogh, A., Dunlop, M. W., … TanDokoro, R. (2004). Transport of solar wind into Earth's magnetosphere through rolled-up Kelvin-Helmholtz vortices. *Letters to Nature*, *430*, 755–758. https://doi.org/10.1038/nature02799

Hasegawa, H., Retinò, A., Vaivads, A., Khotyaintsev, Y., André, M., Nakamura, T. K. M., … Canu, P. (2009). Kelvin-Helmholtz waves at the Earth's magnetopause: Multiscale development and associated reconnection. *Journal of Geophysical Research*, *114*, A12207. https://doi.org/10.1029/2009JA014042

Hietala, H., Drake, J. F., Phan, T. D., Eastwood, J. P., & McFadden, J. P. (2015). Ion temperature anisotropy across a magnetotail reconnection jet. *Geophysical Research Letters*, *42*, 7239–7247. https://doi.org/10.1002/2015GL065168

Hones Jr., E. W., Higbie, P. R., & Palmer, I. D. (1976). Energetic protons of magnetospheric origin in the plasma sheet associated with substorms. *Journal of Geophysical Research*, *81*, 3866–3874. https://doi.org/10.1029/JA081i022p03866

Hwang, K.-J., Kuznetsova, M. M., Sahraoui, F., Goldstein, M. L., Lee, E., & Parks, G. K. (2011). Kelvin-Helmholtz waves under southward interplanetary magnetic field. *Journal of Geophysical Research*, *116*, A08210. https://doi.org/10.1029/2011JA016596

Johnson, J. R., & Cheng, C. Z. (1997). Kinetic Alfvén waves and plasma transport at the magnetopause. *Geophysical Research Letters*, *24*, 1423–1426. https://doi.org/10.1029/97GL01333

Johnson, J. R., & Cheng, C. Z. (2001). Stochastic ion heating at the magnetopause due to kinetic Alfvén waves. *Geophysical Research Letters*, *28*, 4421–4424. https://doi.org/10.1029/2001GL013509

Johnson, J. R., & Wing, S. (2009). Northward interplanetary magnetic field plasma sheet entropies. *Journal of Geophysical Research*, *114*, A00D08. https://doi.org/10.1029/2008JA014017

Johnson, J. R., Cheng, C. Z., & Song, P. (2001). Signatures of mode conversion and kinetic Alfvén waves at the magnetopause. *Geophysical Research Letters*, *28*, 227–230. https://doi.org/10.1029/2000GL012048

Kavosi, S., & Raeder, J. (2015). Ubiquity of Kelvin-Helmholtz waves at Earth's magnetopause. *Nature Communications*, *6*, 7019. https://doi.org/10.1038/ncomms8019

Laakso, H., Taylor, M., & Escoubet, C. P. (2010). The cluster active archive. In *Studying the Earth's space plasma environment, Astrophysics and Space Science Proceedings*, (pp. XX, 489). Noordwijk, Netherlands: Springer. https://doi.org/10.1007/978-90-481-3499-1

Lee, L. C., Johnson, J. R., & Ma, Z. W. (1994). Kinetic Alfven waves as a source of plasma transport at the dayside magnetopause. *Journal of Geophysical Research*, *99*, 17405. https://doi.org/10.1029/94JA01095

Ma, X., & Otto, A. (2014). Nonadiabatic heating in magnetic reconnection. *Journal of Geophysical Research: Space Physics*, *119*, 5575–5588. https://doi.org/10.1002/2014JA019856

Miura, A., & Pritchett, P. L. (1982). Nonlocal stability analysis of the MHD Kelvin-Helmholtz instability in a compressible plasma. *Journal of Geophysical Research*, *87*, 7431–7444. https://doi.org/10.1029/JA087iA09p07431

Moore, T. W. (2012). Identifying signatures of plasma waves and reconnection associated with Kelvin-Helmholtz activity (Master's thesis). Embry-Riddle Aeronautical University.

Moore, T. W., Nykyri, K., & Dimmock, A. P. (2016). Cross-scale energy transport in space plasmas. *Nature Physics*, *12*, 1164–1169.

Nykyri, K. (2013). Impact of MHD shock physics on magnetosheath asymmetry and Kelvin-Helmholtz instability. *Journal of Geophysical Research: Space Physics*, *118*, 5068–5081. https://doi.org/10.1002/jgra.50499

Nykyri, K., & Dimmock, A. (2016). Statistical study of the ULF Pc4–Pc5 range fluctuations in the vicinity of Earth's magnetopause and correlation with the low latitude boundary layer thickness. *Advances in Space Research*, *58*, 257–267. https://doi.org/10.1016/j.asr.2015.12.046

Nykyri, K., & Otto, A. (2001). Plasma transport at the magnetospheric boundary due to reconnection in Kelvin-Helmholtz vortices. *Geophysical Research Letters*, *28*, 3565–3568. https://doi.org/10.1029/2001GL013239

Nykyri, K., & Otto, A. (2004). Influence of the Hall term on KH instability and reconnection inside KH vortices. *Annales Geophysicae*, *22*, 935–949. https://doi.org/10.5194/angeo-22-935-2004

Nykyri, K., Otto, A., Lavraud, B., Mouikis, C., Kistler, L. M., Balogh, A., & Rème, H. (2006). Cluster observations of reconnection due to the Kelvin-Helmholtz instability at the dawnside magnetospheric flank. *Annales Geophysicae*, *24*, 2619–2643. https://doi.org/10.5194/angeo-24-2619-2006

Otto, A., & Fairfield, D. H. (2000). Kelvin-Helmholtz instability at the magnetotail boundary: MHD simulation and comparison with Geotail observations. *Journal of Geophysical Research*, *105*, 21,175–21,190. https://doi.org/10.1029/1999JA000312

Rème, H., Bosqued, J. M., Sauvaud, J. A., Cros, A., Dandouras, J., Aoustin, C., … Balsiger, H. (1997). The Cluster Ion Spectrometry (CIS) experiment. *Space Science Reviews*, *79*, 303–350.

Rezeau, L., Morane, A., Perraut, S., Roux, A., & Schmidt, R. (1989). Characterization of Alfvenic fluctuations in the magnetopause boundary layer. *Journal of Geophysical Research*, *94*, 101–110. https://doi.org/10.1029/JA094iA01p00101

Runov, A., Angelopoulos, V., Sitnov, M. I., Sergeev, V. A., Bonnell, J., McFadden, J. P., … Auster, U. (2009). THEMIS observations of an earthward-propagating dipolarization front. *Geophysical Research Letters*, *36*, L14106. https://doi.org/10.1029/2009GL038980

Sonnerup, B. U. Ö., & Scheible, M. (1998). Minimum and maximum variance analysis. In G. Paschmann, & P. W. Daly (Eds.), *Analysis methods for multi-spacecraft data, ISSI scientific report* pp. 185). Hallerstrasse 6, CH-3012 Bern, Switzerland: The International Space Science Institute.

Stasiewicz, K., Bellan, P., Chaston, C., Kletzing, C., Lysak, R., Maggs, J., … Wahlund, J.-E. (2000). Small scale Alfvénic structure in the aurora. *Space Science Reviews*, *92*, 423–533.

Taylor, M. G. G. T., Lavraud, B., Escoubet, C. P., Milan, S. E., Nykyri, K., Dunlop, M. W., … Zhang, T. L. (2008). The plasma sheet and boundary layers under northward IMF: A multi-point and multi-instrument perspective. *Advances in Space Research*, *41*, 1619–1629. https://doi.org/10.1016/j.asr.2007.10.013

Walsh, B. M., Sibeck, D. G., Wang, Y., & Fairfield, D. H. (2012). Dawn-dusk asymmetries in the Earth's magnetosheath. *Journal of Geophysical Research*, *117*, A12211. https://doi.org/10.1029/2012JA018240

Wang, C.-P., Gkioulidou, M., Lyons, L. R., & Angelopoulos, V. (2012). Spatial distributions of the ion to electron temperature ratio in the magnetosheath and plasma sheet. *Journal of Geophysical Research*, *117*, A08215. https://doi.org/10.1029/2012JA017658

Wilder, F. D., Ergun, R. E., Schwartz, S. J., Newman, D. L., Eriksson, S., Stawarz, J. E., … Magnes, W. (2016). Observations of large-amplitude, parallel, electrostatic waves associated with the Kelvin-Helmholtz instability by the Magnetospheric Multiscale Mission. *Geophysical Research Letters*, *43*, 8859–8866. https://doi.org/10.1002/2016GL070404

Wing, S., & Newell, P. T. (2002). 2D plasma sheet ion density and temperature profiles for northward and southward IMF. *Geophysical Research Letters*, *29*(9), 1307. https://doi.org/10.1029/2001GL013950

Wing, S., Johnson, J. R., Newell, P. T., & Meng, C.-I. (2005). Dawn-dusk asymmetries, ion spectra, and sources in the northward interplanetary magnetic field plasma sheet. *Journal of Geophysical Research*, *110*, A08205. https://doi.org/10.1029/2005JA011086

Woolliscroft, L. J. C., Alleyne, H. S. C., Dunford, C. M., Sumner, A., Thompson, J. A., Walker, S. N., … Gough, M. P. (1997). The digital wave-processing experiment on Cluster. *Space Science Reviews*, *79*, 209–231.

Yan, G. Q., Mozer, F. S., Shen, C., Chen, T., Parks, G. K., Cai, C. L., & McFadden, J. P. (2014). Kelvin-Helmholtz vortices observed by THEMIS at the duskside of the magnetopause under southward interplanetary magnetic field. *Geophysical Research Letters*, *41*, 4427–4434. https://doi.org/10.1002/2014GL060589

Yao, Y., Chaston, C. C., Glassmeier, K.-H., & Angelopoulos, V. (2011). Electromagnetic waves on ion gyro-radii scales across the magnetopause. *Geophysical Research Letters*, *38*, L09102. https://doi.org/10.1029/2011GL047328